Mapping of Sedimentary Bodies by 3D Seismic Reflection Data

Application to the pre-Messinian Ebro Margin

A project submitted in partial fulfillment of the
requirements for the degree of

MASTER OF SCIENCE

in

GEOPHYSICS

by

Alejandra Lago Cameselle

Universitat de Barcelona & Universitat Ramón Llull
Barcelona, Spain

September 2010

Tutor: **Dr. Roger Urgeles Esclasans**
Barcelona Center for Subsurface Imaging (BCSI)
Consejo Superior de Investigaciones Científicas (CSIC)
Passeig Marítim de la Barceloneta, 37-49. E-08003 Barcelona (Spain)

A miña avóa Marina,
Por tódo-lo que coidaches
e segues a coidar de min.

Acknowledgements

En primeiro lugar gustaríame agradecerlle ós meus pais e ó meu irmáo apoio incondicional que me brindaron durante os meus estudios, facendo deste camiño algo máis levadeiro. Sen eles nin isto nin nada fose posible.

Grazas a Daniel, por estar máis preto de min canto máis difíciles se puñan as cousas, e pola paciencia infinita que tivo e que sei que terá. Á miña Miriam, simplemente "*grazas"*, ti xa sabes porque. E grazas ó meu gran amigo Alpi, por "enganarme" con isto da sísmica e estar ó meu carón sempre que ó precisei.

Grazas á miña “familia de Barcelona”, por compartir tantos días bos, pero tamén polas horas que compartimos sen durmir. Grazas tamén ós compañeiros do CMIMA, por facerme sentir unha máis dende os primeiros intres e porque todos e cada un deles ofrecéronme a súa axuda durante todos estes meses.

Grazas en especial ó meu titor, Roger Urgeles, pola súa confianza en min e sobre todo pola súa paciencia e mais por tódo-lo tempo que me dedicou sempre que o precisei.

E grazas, por suposto, á tóda-las persoas que ó longo do tempo han pasado pola miña vida achegando o seu graníño de area.

UNIVERSITAT DE BARCELONA & UNIVERSITAT RAMON LLULL
Master in Geophysics

Master's Thesis

Abstract

Mapping of Sedimentary Bodies by 3D Seismic Reflection Data: Application to the pre-Messinian Ebro Margin

by

Alejandra Lago Cameselle

Three-dimensional (3D) seismic reflection profiling is one of the most advanced technologies used in offshore and onshore geophysics. It is needed for a wide range of investigations, most often carried out by the hydrocarbon industry, in inshore, coastal, and deep ocean environments. Three-dimensional seismic reflection profiling, provides high-resolution images of the subsurface that allow solving detailed structural and stratigraphic conditions. The implementation of seismic attributes, such as amplitude or coherence, has improved our capacity to visualize and interpret features such as sedimentary patterns (e.g., channel systems) or faults and fractures in any orientation.

In this project, we used 2700 km^2 of 3D seismic reflection data with the aim of mapping the Miocene sedimentary bodies deposited in front of the Ebro Delta. From these data we try to 1) offer new constrains on the geomorphological evolution of the Ebro Margin, 2) provide evidences of a possible pre-Messinian connexion between the Ebro Basin and the Mediterranean Sea, which is still the subject of intense debate, and, 3) determine whether all prograding clinoforms below the Messinian Erosion Surface (MES) are actually pre-Messinian or some were formed during the Messinian.

Five seismic surfaces were mapped between the Top Oligocene and the MES along the 3D seismic volume, including the two boundaries and three intra-Miocene horizons to establish accurate stratigraphic markers for the mapped area as a whole. The 3D seismic data display a major NE-SW oriented horst-and-graben structure developed in an extensional context during the upper Oligocene-early Miocene (Sàbat *et al.*, 1997; Roca *et al.*, 1999). The study of the depocentres shows that the initial sedimentary transport started filling the deepest troughs from north-northwest during the syn-rift stage.

The increasing sedimentation, together with the attenuation of the tectonic activity, led to a progressive filling of the grabens, subsequent spreading and final onlapping of the structural highs. This caused the development of sigmoidal clinoforms that evolved in a progradational system. This increase of the sediment rate, together with the change in the transport direction from longitudinal (N-NW) to transversal (E-NE) observed from the study of the depocentres, are presumably indicative of the existence of a pre-Messinian Ebro River.

Moreover, the subsequent Messinian Salinity Crisis truncated the evolution of the Ebro Margin, which became dominated by a major fluvial system identified as the Messinian Ebro River. The high-equilibrium conditions reached by this drainage network also support the idea of a capture of the Ebro Basin by a relative small river prior to the Messinian drawdown.

Table of Contents

Index of Figures

Index of Tables

Chapter 1

Introduction

3D seismic techniques have promoted the large and rapid development of new visualization and seismic analysis techniques, including 3D seismic attributes and advent of new research fields such as seismic geomorphology. Because 3D seismic surveys provide a really good resolution of subsurface structures, it is an excellent geophysical method for the study of the sedimentary processes in marine transition areas such as the Ebro Margin.

The Ebro Margin is characterized by a complex pattern of well-developed margin-scale clinoforms (Dañobeitia *et al.*, 1990; Bartrina *et al.*, 2002) and the Ebro River has played a major role in the development of these sedimentary structures, supplying and distributing large amounts of sediments (Bartrina *et al.*, 1992). One of the main problems in determining the complete evolution of this area is the establishment of the timing and processes related to the initial connection between the Ebro Basin and the Mediterranean Sea because of the lost of a great part of the sedimentary record during the Messinian Salinity Crisis (MSC).

Some authors (i.e. Ribba *et al.* (1983) and Bartrina *et al.* (1992), and later Babault *et al.* (2006)) offered the hypothesis of capture of the Ebro Basin by some small stream during the backward erosion associated with the sea level drop that occurred during the MSC. Later, Evans and Arche (2002), García-Castellanos *et al.* (2003), and more recently Arche *et al.* (2010) or Urgeles *et al.* (2010) have raised several concerns on the validity of this idea, providing the hypothesis of a pre-Messinian connection between a proto-Ebro river and the Mediterranean Sea supported by the evidence of enhanced sedimentation rates and deltaic progradations prior to the Messinian event.

From the analysis of sedimentary bodies along 2700 km^2 of 3D seismic reflection data, this study attempts to contribute to 1) a better understanding of the sedimentary processes and geomorphological evolution of the Ebro Margin during the

Miocene, 2) provide new lights on the timing of the connection between the Ebro Basin and the Mediterranean Sea and 3) determine whether all prograding clinoforms below the Messinian Erosional Surface (MES) are actually pre-Messinian or some were formed during the Messinian.

Chapter 2

Geological Framework

The present 3D seismic survey covers an area of 2700 km^2 of the Ebro Margin, NW Mediterranean Sea (Fig. 1), opposite the delta generated by the Ebro River, which covers an area of about 320 km^2.

2.1. The Ebro Margin

The Ebro Margin is a passive continental margin located in northeastern Spain. It was developed as the western branch of the Valencia Trough, between the Iberian Peninsula and the Balearic Promontory (Fig. 1).

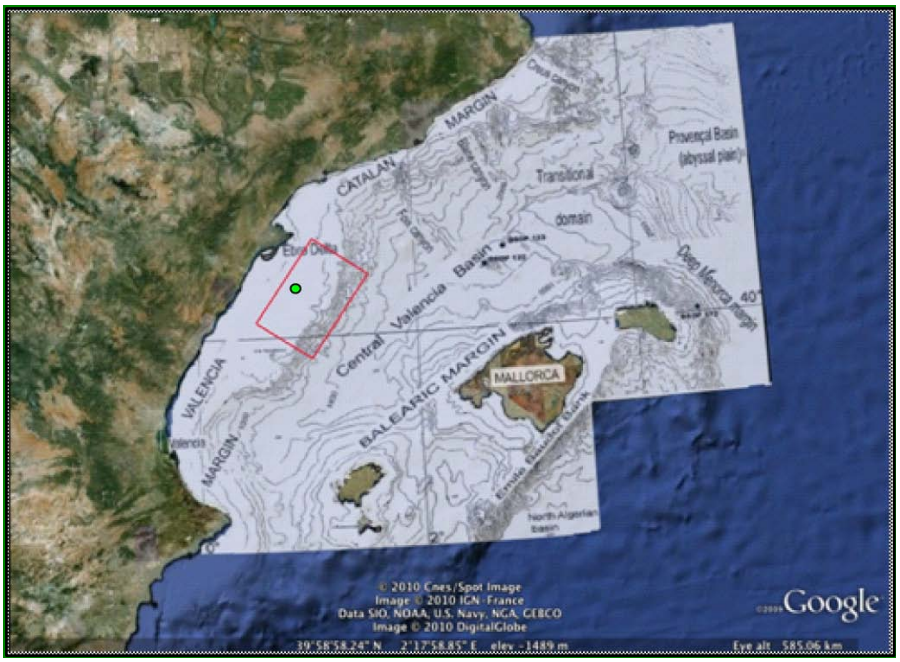

Fig. 1. Location of the study area in the northwestern Mediterranean Sea. Red box and the green circle (not to scale) represent the location of the 3D seismic survey used in this study and the location of the FORNAX-1 well, respectively(adapted from Maillar *et al.*, 2006).

The extension responsible for the formation of this trough started in southern France during the Early Oligocene, affecting the northeastern Valencia Trough during

the Chattian-Aquitanian in the form of an aborted rift associated to back-arc processes (Olivet, 1996; Duggen *et al.*, 2003). The process was attenuated when Betic compression affected the Balearic Islands during the Burdigalian-Langhian (Geel, 1995).

In this context, the Ebro Margin (Fig. 1) developed as an extensional fault system with a northeast-southwestern trending horst-and-graben structure resulting from tectonic inversion of previous Paleogene reverse faults of the Catalan Coastal Ranges (Sàbat *et al.*, 1997; Roca *et al.*, 1999). The opening began during the Oligocene and continued until the Middle Miocene. During the Early Miocene, coinciding with the rift stage, deposition was mainly controlled by the extensional fault system.

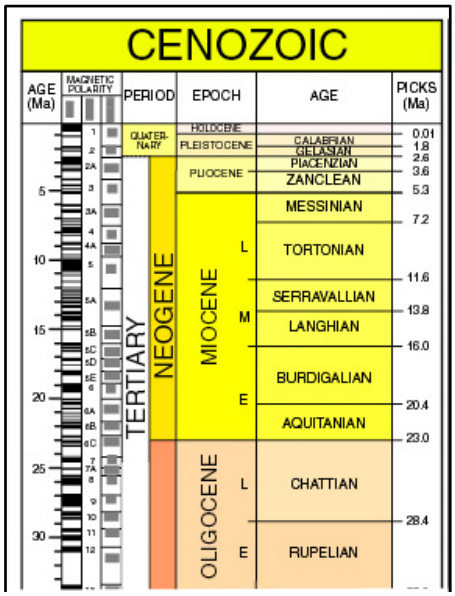

Fig. 2. Geologic Time Scale referred to the study period.

The post-rift stage began in the Langhian with the attenuation of the tectonic activity and continued until the Late Miocene. During this time, deposited material overfilled post-rift subsidence accommodation space and caused progradation of the shelf and talus sediments. As consequence of the tectonic activity reduction and the large sediment supply from the Iberian Peninsula the topography of the Ebro Margin was subdued (García-Siñeriz *et al.*, 1979).

In terms of this Neogene evolution, the combination of the glacio-eustatic sea level fall with the uplift of the Gibraltar region during the Lower to Upper Messinian resulted in the isolation of the Mediterranean Basin from the Atlantic Ocean. This

situation triggered the desiccation of the Mediterranean Sea in what is known as the Messinian Salinity Crisis (MSC), which lasted from 5.6 Ma to 5.33 Ma (Hsü *et al.*, 1973; Clauzon *et al.*, 1996; Krijgsman *et al.*, 1999).

As a result of this event, the sea level dropped dramatically between 1500 and 2700 m (Ryan, 1976; Blanc, 2006), resulting in basin subaerial exposure, strong incision of the fluvial systems and creation of deep canyons. The phase of maximum erosion lasted 90-300 Kyr.

During the early Pliocene, about 5.33 Ma ago, the tectonic subsidence of the Gibraltar Strait, probably in combination with sill erosion (Loget and Van Den Driessche, 2006) and sea level rise, caused the flooding of the Mediterranean basin and the re-establishment of normal marine conditions. Transgression resulted in deposition of marine clay over the margin (Stampfli and Höcker, 1989). Because of the sudden sea level rise, between a few months and two years (García-Castellanos *et al.*, 2009), the Messinian Erosional Surface (MES) was largely preserved.

Plio-Pleistocene sedimentation is characterized by a megasequence, known as Ebro Group, strongly influenced by the topographic relief generated during the MSC (Nelson and Maldonado, 1990). The stratigraphic pattern during deposition of this megasequence results from progradation of the slope in response to large sediment supply from the Ebro River, which resulted in a wide continental shelf extended more than 70 km into the Valencia Trough, being one of the widest continental shelf in the Western Mediterranean Sea (Dañobeitia *et al.*, 1990).

2.2. The Ebro Basin

The Ebro basin is the largest Cenozoic foreland basin in northeast Spain. It results from the tectonic collision of the Iberian and European plates during the early Paleocene, being mainly controlled by the structural development of the ranges surrounding it: the Pyrenees to the north, the Iberian Ranges to the south and the Catalan Coastal Ranges to the east (Fig. 3). The uplift of the Pyrenees in the upper Eocene interrupted the communication between the Ebro Basin and the Atlantic Ocean.

The timing of aperture towards the Mediterranean has been and is still the subject of intense debate. Two major hypothesis are considered: 1) Riba *et al.* (1983), Bartrina *et al.* (1992) or Babault *et al.* (2006) suggested capture of the Ebro Basin associated with the MSC, when the sea level drop caused backward erosion of Mediterranean rivers. 2) A pre-Messinian connection between a proto-Ebro river and the Mediterranean Sea occurred 13-8.5 Ma ago, in the Serravallian-Tortonian (Evans and Arche, 2002; García-Castellanos *et al.*, 2003; Arche *et al.*, 2010; Urgeles *et al.*, 2010).

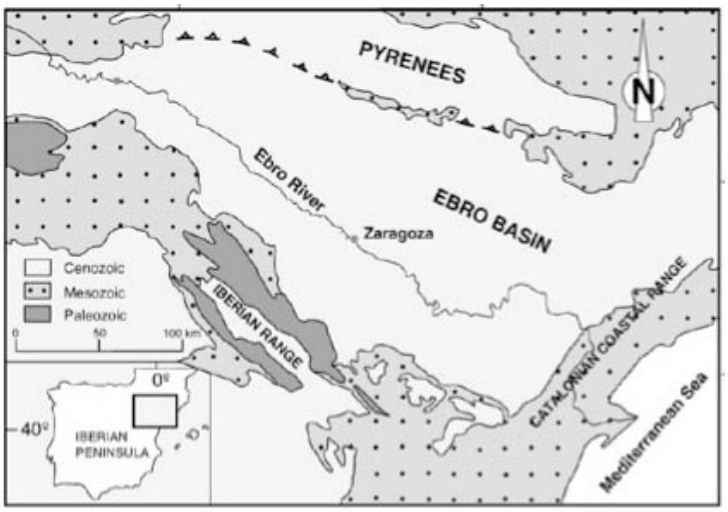

Fig. 3. Geological map of the Ebro Basin (NE Spain) surrounding by the three main ranges: Pyrenees, Catalan Coastal Ranges and Iberian Range (Luzón *et al.*, 2008).

The most commonly invoked mechanism responsible for the capture includes erosion by a small mountain river on the southeastern side of the Catalan Coastal Ranges, in combination with one or more of the following large-scale processes: 1) partial tectonic deconstruction of the CCR; 2) flexural flank uplift of the CCR; 3) sediment overfill of the lake; and 4) lake level rise related to a long-term climatic change to wetter conditions.

Since capture, the Ebro fluvial system has evolved producing significant erosion of the Tertiary sediments. Nowadays, Quaternary sediments, which are mainly fluvial stepped terraces and pediment levels, cover one third of the Tertiary sediments (Gutierrez and Peña, 1989).

Chapter 3

Design and Acquisition of 3D Seismic Reflection Survey.

The seismic reflection is a method of geophysical exploration that uses the principles of seismology to estimate the properties of the Earth's subsurface from reflected seismic waves. This information is obtained from the return of energy in each acoustic impedance change that elastic waves (pulses) encounter travelling through the media, obtaining a representative image of the internal structure of the Earth (International Association of Geophysical Contractors [IAGC], March 2002).

Marine seismic acquisition system consists of a sound source towed behind the vessel within a few meters of the surface that produces sound pulses at a controlled frequency range at set time intervals. The waves, partially reflected in the sea floor, return to the surface and are recorded by hydrophones towed further behind the vessel in a streamer (Fig. 4).

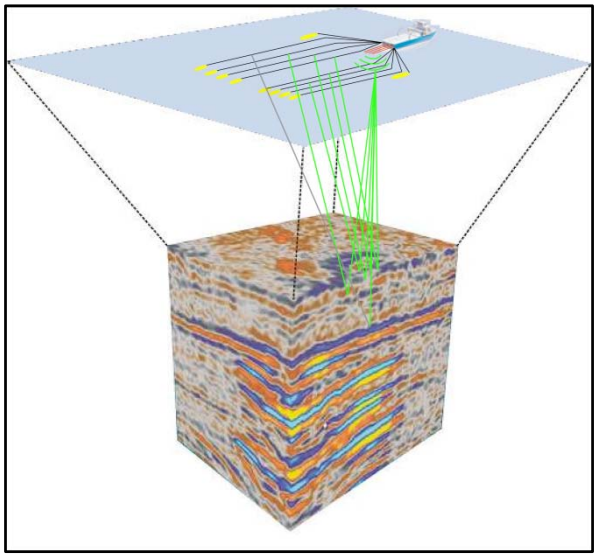

Fig. 4. 3D seismic survey, showing simplified configuration of seismic vessel and subsurface cube of data

It is a non-destructive method that allows the access to some earth zones that can't be reached by other methods, like geological structures beneath the deep sea or the

lower crust, giving a good resolution. The two primary exploration environments are (International Association of Geophysical Contractors [IAGC], March 2002)

- Onshore or Land Exploration, including Antarctic Ice Sheet,
- Offshore or Marine Exploration.

There is a third marine exploration zone, commonly called Shallow Water Exploration, also sometimes referred to as Transition Zone Exploration (TZ) that involves shallow water areas as tidal zones, river estuaries or swamplands.

Although the methodology is substantially different in the three cases, seismic exploration consists of three main stages: data acquisition, processing and interpretation.

3.1. Reflection Theory Review

The transmission of energy in seismic prospecting can be explained by assuming that the Earth has the elastic properties of a solid; hence the type of acoustic wave transmission is elastic wave propagation. Seismic waves created by an explosive source emanate outward from the shot point in a 3D sense (Huygens' Principle) and they may experience different phenomenon as a result of its interaction with the media, the three basic ones are: reflection, refraction or diffraction (Fig. 5). In seismic reflection surveys, the reflection phenomenon is used to obtain information about the Earth's crust (Urick, 1983; Yilmaz, 2001; Stein and Wysession, 2003).

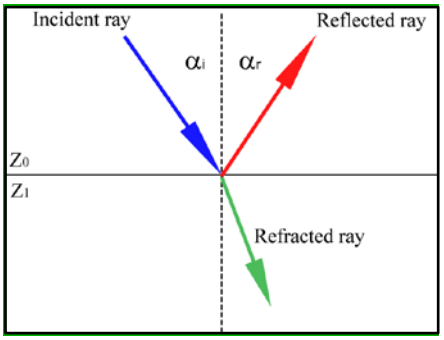

Fig. 5. Refraction and reflection of a ray at the boundary of two different media

Seismic reflection is the change in direction of a wavefront at a boundary between two media with different acoustic impedances. The *acoustic impedance* (*Z*) is

defined as the product of the mass density of the rock (ρ) and the wave velocity (V) (Urick, 1983; Yilmaz, 1987)

$$Z = V\rho$$

The energy reflected from an impedance boundary is proportional to the amplitude of the sound impulse produced by the source and the magnitude of the impedance contrast. For a wave that hits a boundary at normal incidence, the expression for the *reflection coefficient* (R_c) is

$$R_c = \frac{Z_1 - Z_0}{Z_1 + Z_0}$$

where Z_i is the impedance of the mediums. The amount of energy reflected is independent of the sign of the reflection coefficient (Urick, 1983; *Yilmaz, 2001*; Stein and Wysession, 2003).

The amplitude and polarity of the reflections depend on the acoustic properties of the material on both sides of the discontinuity. The relationship among incident amplitude (A_i), reflected amplitude (A_r) and reflection coefficient (R_c) is

$$A_r = R_c \cdot A_i$$

On the other hand, the time it takes for a reflection from a particular boundary to arrive at the receiver and back is called the *Two Way Travel-Time* (*twtt*) and may be used to estimate the depth to the reflector (Stein and Wysession, 2003).

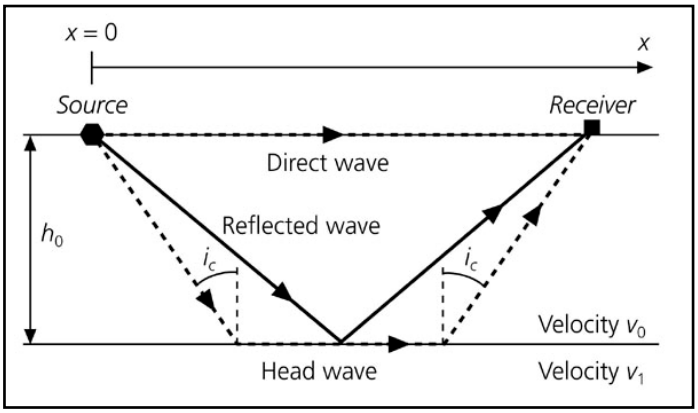

Fig. 6. Ray paths for a layer over a half space (Stein and Wysession, 2003)

The curve for this estimation can be found by noting that *x/2* and h_0 form two sides of a right triangle (Fig. 6), so

$$TWT = 2\left(x^2/_4 + h_0^2\right)^{1/_2} \Big/ v_0$$

By observing changes in the impedances, seismologists can infer changes in the properties of the rocks at the interface, areas of structural deformation or they can correlate reflection events.

3.2. 3D Seismic Marine Geophysical Surveys

The seismic technique was originally developed by the oil exploration industry in the 1930's. The arrival of the 2D multi-fold (common-mid-point) surveys, jointly with fast development of instrumentation, computers and data processing techniques, greatly increased the resolution of seismic data and the accuracy of the subsurface images. However, it was not until the 1980's, with the arrival of 3D reflection, that seismic surveys began to resolve the detailed subsurface structural and stratigraphic conditions. The result is a volume, or cube, of seismic data that was sampled (Fig. 7) from a narrow range of angles.

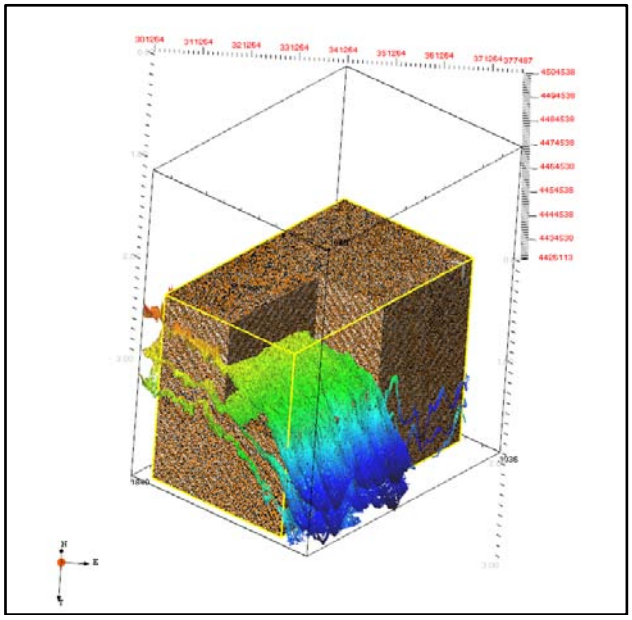

Fig. 7. 3Damplitude data-cube showing strike and dip profiles, and three surfaces rendering of MES, PreMess2 and Top Oligocene (from top to bottom).

3.2.1. Basic 3D Terminology and Parameters in Seismic Surveys

The parameters used for each acquisition project depends on a significant number of variables specific to the particular area and must be estimated as input when designing the 3D survey (Chaouch and Mari, 2006):

- Box (S_b): Area encompassed by two consecutive receiver lines (Ry) and two consecutive source lines (Sx). The box area will be

$$S_b = R_y \cdot S_x$$

- *Directions*: There are two main directions to be considered

  In-line direction: the shooting direction

  Cross-line direction: the orthogonal direction to the vessel track

- *Offset*: Horizontal distance from source to receiver (Fig. 8). It creates a delay, or moveout, in the arrival time of a reflection that can be corrected before stacking and can be used to determine velocity. For 3D surveys, the contribution of each class of offset is different: about 57% for far offsets, 33% for mid offsets and 10% for near offsets. This percentage distribution improves the suppression of multiples because it will reduce the noise associated with the near offsets (ground roll, air blast, source generated noise...).

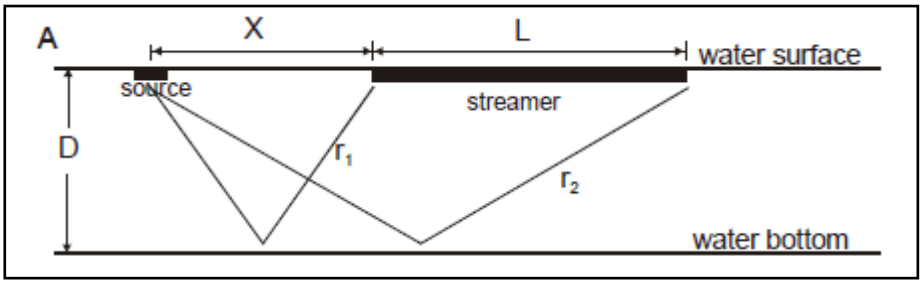

Fig. 8. Schematic source-receiver geometry where D is the water depth, X is the source-receiver offset and L is the maximum array length (Modified from Verbeek and McGee, 1995)

- *Common-mid-point (CMP)*: For 2D seismic acquisition, it is the point located in the middle of different source-receiver pairs which reflection corresponds to the same subsurface point.

- *Bin (b)*: Basic building block for the rest of the survey (Fig. 9). Bins are commonly square or rectangular and define the spatial resolution of the data sampling. The basic sampling theorem that applies to the bin is

$$b = \frac{V_{min}}{(4 \cdot F_{max} \cdot \sin\theta)}$$

where V_{min} is the minimum velocity, F_{max} is the maximum frequency expected and θ is the maximum dip.

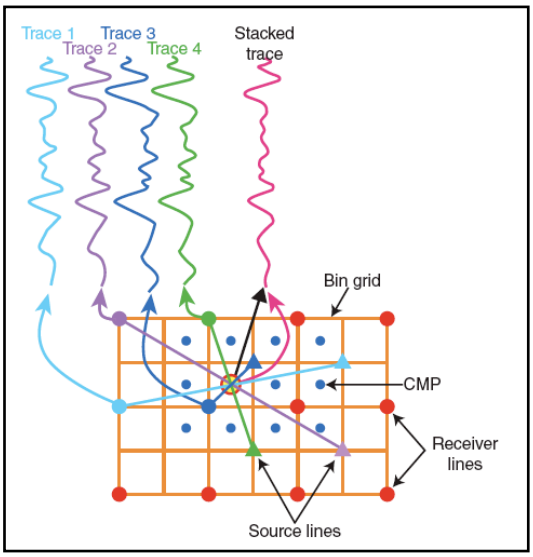

Fig. 9. Basic parameters in 3D seismic surveys. Traces are generated in the middle of source-receiver pairs, and the number of traces within a bin corresponds with the 3D fold (Chaouch and Mari, 2006).

- *Migration aperture (ΔX)*: Expansion of the survey area that must be added in order to correctly migrate dipping layers and diffracted energy located at the edge of the target area (Fig. 10). The extent of the survey must be increased proportionally to the depth (Z) by

$$\Delta X = Z \cdot \tan\theta$$

In short, to successfully plan a 3D survey three areas must be considered to ensure an optimum quality of the results.

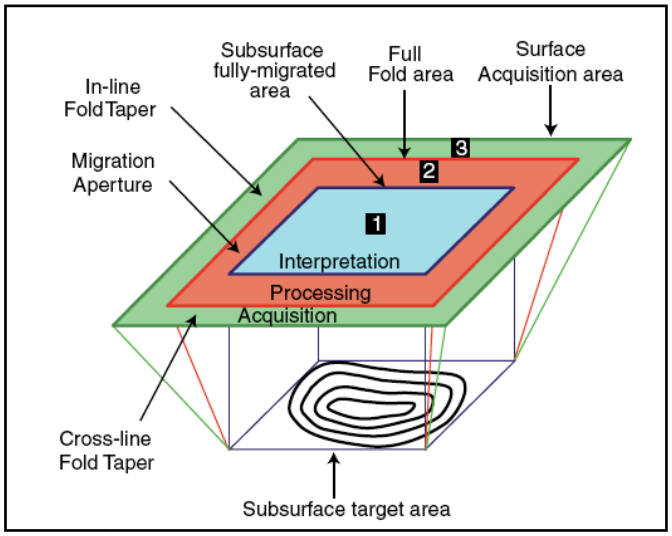

Fig. 10. 3D seismic areas. 1) Subsurface Full Fold Fully Migrated area; 2) Full Fold area; 3) Surface Acquisition area (Chaouch and Mari, 2006).

The first area (Fig. 10) corresponds to the subsurface target area that must be fully migrated and will be interpreted after complete processing. It is called *Subsurface Full Fold Fully Migrated Area*. The second area will influence the processing by collapsing the energy lying in it to the edge of the fully migrated area (area 1). It is called *Full Fold Area*. The last surface is the complete Surface *Acquisition Area* and is needed for operational requirements (Chaouch and Mari, 2006).

3.3. Marine Seismic Reflection Sources

All acoustic sources used in marine seismic profiling have to convert stored energy into a pressure wave. In the marine environment the choice of the source will depend on the known sub-area geology, the previous data, the depth of interest, the desired frequency output and so on.

There is a trade-off between penetration, which demands lower frequencies, and resolution, which requires greater bandwidths (higher frequencies). Vertical seismic *resolution* is defined as the minimum separation between two interfaces so that they can be identified as two interfaces rather than one (Avseth *et al.*, 2005). A stratigraphic layer can be resolved in seismic data if the layer thickness is larger than a quarter of a wavelength. The wavelength is given by:

$$\lambda = {}^{V}/_{f}$$

where *V* is the interval velocity of the layer, and *f* is the frequency of the seismic wave. *Frequency* is defined as the rate of repetition of complete wavelengths of seismic waves measured in cycles per second, or hertz. As a field approximation, the maximum frequency expected will be (Chaouch and Mari, 2006):

$$F_{max} = \frac{150}{TWT}$$

There are now three types of seismic source: airguns, waterguns and vibrators (explosives are an historic source). The most used marine seismic source for geophysical exploration is the airgun, because the pulses are predictable, repeatable and controllable, and it uses compressed air, which is cheap and readily available (SCAR Ad Hoc Group on marine acoustic technology and environment, July 2002).

An *airgun* is defined as a mechanical device that stores high-pressure air in a chamber and releases it suddenly through ports in response to an electrical trigger (Fig. 11). When the air escapes, part of the energy is released as a sound wave, travelling into the subsurface and reflecting back to the hydrophones. The pulse rise time is of the order of a few milliseconds (Dragoset, 2000; Landro and Amundsen, 2010).

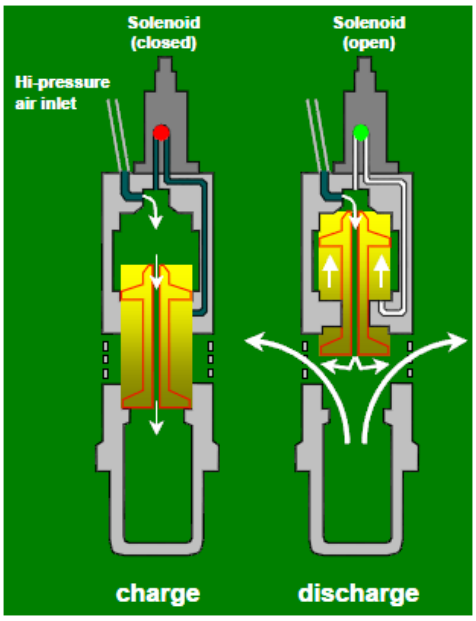

Fig. 11. Airgun mechanism. The airgun comprises two high-pressure air chambers. When an electrical pulse is sending, solenoid valve opens; air into upper chamber flows to the underside of the triggering piston and the high-pressure air in the lower chamber is discharge into the surrounding water. (International Association of Geophysical Contractors [IAGC], March 2002)

Vessels for marine seismic surveys are capable of towing one or more seismic cables with multiple airguns, called *arrays*, behind the vessel. These arrays generally consists of 3-6 sub-arrays called strings, each string containing 4-8 individual guns, so that the array usually involves between 12 and 48 guns (Offshore Energy Environmental Research Association [OEER]; Landro and Amundsen, 2010). The main purpose of clustering is to improve signal characteristics because it increases the power of the source and because guns with different volumes will have different bubble periods, leading to a constructive summation of the primary peak and destructive summation of the bubble amplitudes (Dragoset, 2000; Caldwell and Dragoset, 2000).

The airguns hang in the sea beneath floats between 3 m and 10 m below the sea surface, generally at about 6 m. The guns fire every 10-15 seconds and the energy is sent out mainly directed vertically downward.

3.4. Marine Seismic Reflection Receivers

In 3D marine seismic reflection surveys the common signal receiving system is the hydrophone, which consists of a pressure sensitive piezo-electric element which produces an output voltage proportional to the change in amplitude of the surrounding pressure field (Urick, 1983). These detectors are normally enclosed in a flexible watertight tube called streamer (Fig. 12), and towed behind the vessel some distance away from the source to try to minimize the noise associated with the ship and the sound sources.

The available streamer length has increased over time, but depends fundamentally on the depth and type of the geological target, varying from 1 to 12 kilometres. Since seismic vessels can tow several streamers in parallel, deployments of 40 or 50 km are becoming more prevalent (International Association of Geophysical Contractors [IAGC], March 2002).

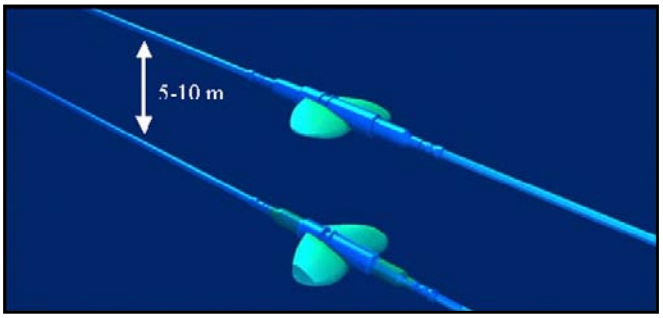

Fig. 12. Streamers are deployed in the same vertical plan at large depths and separated by 5 to 10 m. *Birds* responds to marine currents or to variations introduced by seismic vessel pitching movements. They are normally spaced about 300 m apart from each other (Ikelle and Amundsen, 2005)

Streamer tow depths are a compromise between the need to isolate the streamer from the noise sources and the water layer necessary to obtain an appropriate bandwidth of the data. The typical operational depth range varies from 4 to 5 meters for shallow, high-resolution surveys with "good weather" to 8 to 10 meters for deeper penetration, lower frequency targets. To control the depth to an accuracy of plus or minus 1 meter, an electronically controlled device, called *bird* (Fig. 12), is fitted to the streamer (Bartolomé, 2002; International Association of Geophysical Contractors [IAGC], March 2002).

One of the most critical elements in the 3D seismic method is the positioning of the in-sea equipment. To accurately calculate where subsurface features are located, navigators compute the position of both the sound source and each hydrophone group. To that end, a combination of acoustic networks, compasses and GPS receivers are used (often used with a radio correction commonly known as differential GPS or DGPS).

Chapter 4

Processing of 3D Seismic Data

4.1. General Processing Flux for Seismic Reflection Data

The 3D seismic method has become the main technique in exploration and development of oil and gas fields. Therefore, a great development of algorithms for 3D seismic data processing have taken place, which have now become an integral part of the applications library of processing systems in use today (Yilmaz, 2001). Processing is required because the data collected from the field are not a true representation of the subsurface, so they must be converted to a form that can be used for geological interpretation. Moreover, the full record contains the reflections but also the coherent and random ambient noise that must be eliminated or attenuated in order to enhance the signal to noise ratio (*S/N*).

The data used in this work are part of a 3D seismic survey that covers 2700 $km^2$of seafloor, and acquired by Petroleum Geo Services (PGS) on behalf of British Gas BV in 2002. Together with the seismic data, a series of well logs, including p-wave velocity, share wave velocity and gamma ray, were acquired along the FORNAX-1 well (Fig. 1). These data were already processed, so the accurate steps applied to obtain the final binned 3D seismic volume are unknown. The scarce information available indicates that the seismic data are SEG normal polarity, i.e. an increase in impedance is a positive amplitude. They were processed to near zero phase and migrated with single pass 3D pre-stack time migration resulting in a seismic cube with horizontal grid cells of 12.5x12.5 m and a sampling interval of 4ms (Table 1).

Table 1. Processing survey details

Starting Line	1036
Sample Interval	0.004 sec
Samples per Trace	1750
Bytes/Sample	4
Projection	Universal Transverse Mercator - Zone 31
Ellipsoid / DATUM	International - 1924 / European 1950, Mean Values

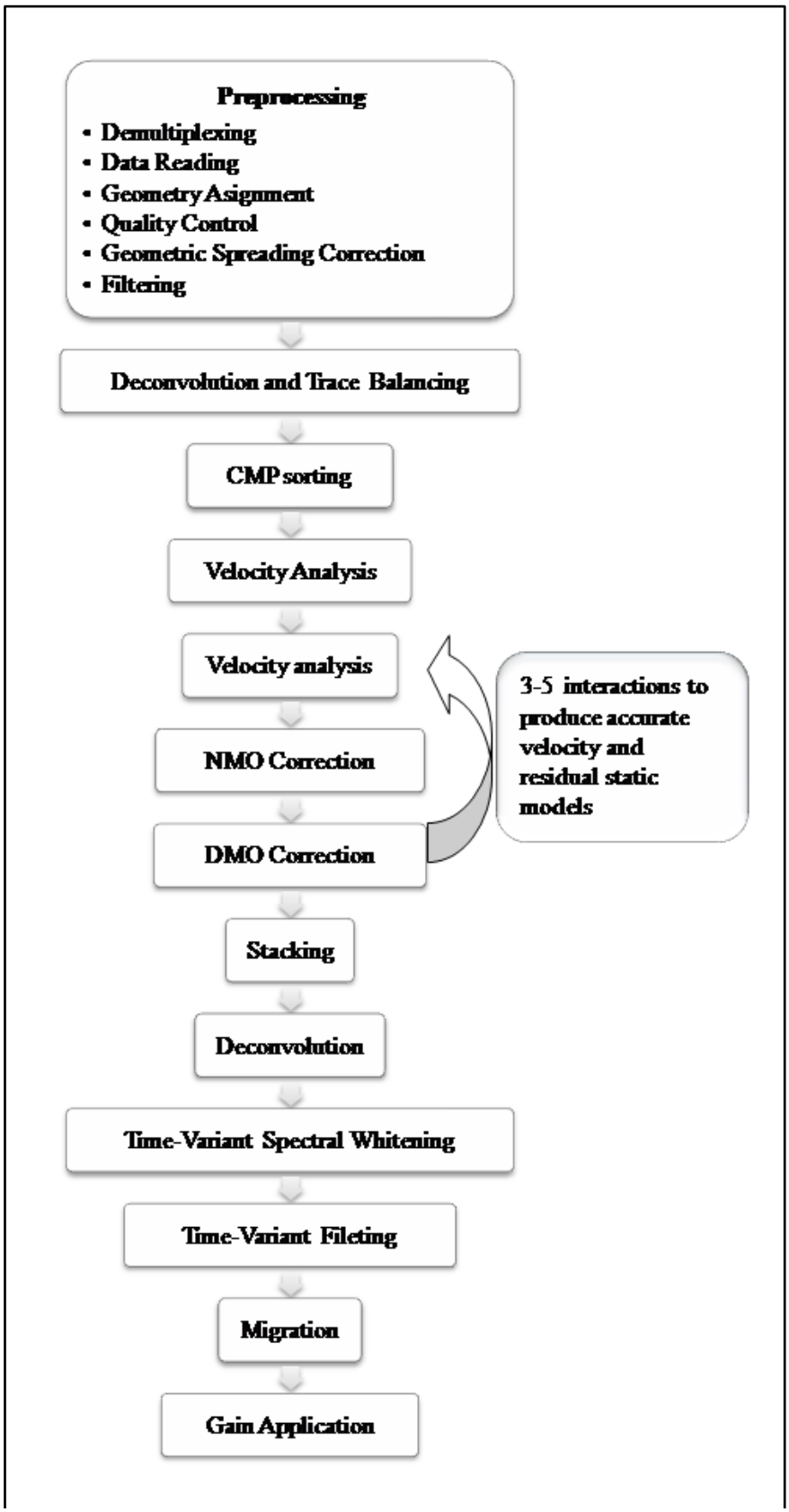

Fig. 13.General scheme for reflection data processing (Modified from Yilmaz, 2001).

Since the processing applied to the data survey is unknown, here a general seismic reflection processing flux will be briefly presented (Fig. 13). The three basic steps of 2D seismic data processing are still apply to 3D processing: deconvolution, stacking and migration. There are also multiple auxiliary processes that help to improve the effectiveness of the primary processes, including: geometric corrections, NMO, DMO, velocity analysis, filtering... (Yilmaz, 2001).

Nevertheless, additional complications can arise in *geometry quality control*, *dip-moveout correction*, *velocity analysis and migration* in 3D seismic processing. As the survey from which the data presented in this study was carried out by means of 3D techniques, differences between 2D and 3D processing will be stressed.

4.2. 3D Geometry Quality Control

In 2D processing, traces are collected into CMP gathers to create a CMP stack, while in 3D processing, traces are collected into bins (common-cell gathers) to create common-cell stacks (Fig. 9). Typical cell sizes for marine surveys are 12.5 x 25 m. Because of that, variations in fold coverage have undesirable effects on velocity estimation, multiple attenuation and amplitude variation with offset (AVO), so analysis and coverage maps are essential to quality control in processing and interpretation. There are four basic considerations in 3D marine acquisition geometry that will determine the correct fold coverage and therefore, the success of the subsequent data processing: cable feathering, 3D binning, crossline smearing and shooting direction (Yilmaz, 2001).

4.2.1. Cable feathering

Receiver cables are subject to a certain amount of sideways drift, called *feathering*, as consequence of the crosscurrents. The angle between the actual cable position and the shot-line direction (the vessel track) is called the *feathering angle*, and is not always constant (Fig. 14) (Yilmaz, 2001).

This causes the midpoints to spread in the crossline direction over subsurface strips (Fig. 14). When data are sorted into common-cell gathers, each cell contains

midpoints associated with more than one source line; therefore it is essential to know the exact vessel and source locations as well as the cable compass readings.

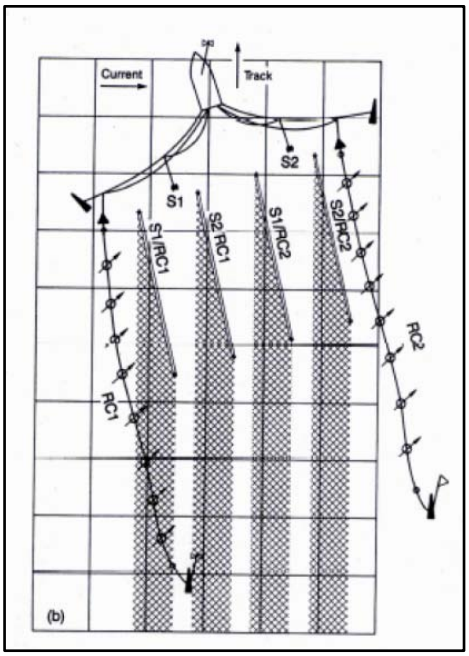

Fig. 14. Feathering and drifting from the shot-line direction caused by crosscurrents. Because points spread in the crossline direction, each cell contains midpoints associated with more than one source line. S1 and S1 represent the dual-source while RC1 and RC2 are the dual-source (Yilmaz, 2001).

There are 8 to 12 digital compasses along a typical marine cable. Readings from this device allow computation of the (*x*,*y*) coordinates of the streamers. Navigation data are analyzed during processing, and quality control is carried out to derive the final shot-receiver locations (Yilmaz, 2001).

4.2. 3D Binning

As it was explained above, processing of 3D seismic data requires binning the recorded data into common-cell gathers. To perform this, a grid (consisting of cells with dimensions of half the receiver group spacing in the inline direction and the line spacing in the crossline direction (Fig. 9)) is superimposed on the survey area. This is equivalent to the CMP in 2D processing.

Since cable shape varies from shot to shot and line-to-line, midpoint distribution within a cell is not necessary uniform and also can vary from cell to cell (Fig. 14 and Fig. 15). These irregularities in geometry can cause problems in processing the 3D seismic data. A slight translation and rotation of the grid imposed on the survey area

sometimes can reduce problems associated with binning because it yields a more uniform midpoint distribution within each cell, and even improve the uniformity of the fold of coverage over the survey area (Yilmaz, 2001).

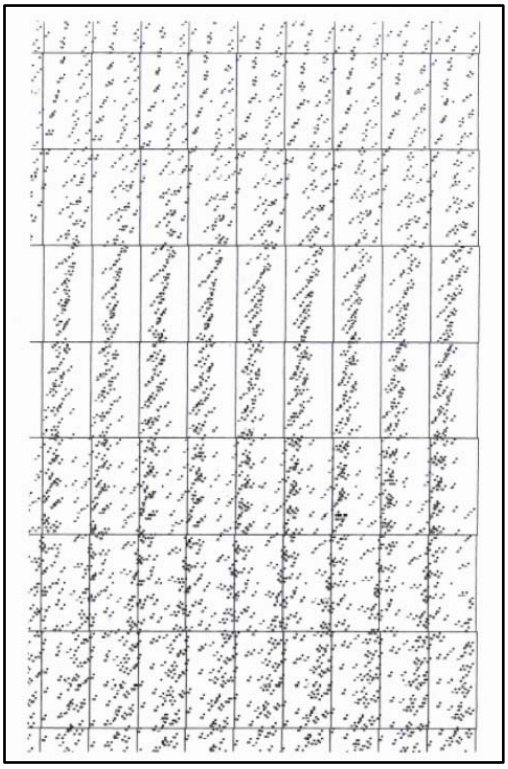

Fig. 15. Midpoints distribution in cells (Yilmaz, 2001)

Furthermore, this process allows the adjustment of the cell size in what is known as *flexible binning*, which includes two main corrections (Yilmaz, 2001):

- More midpoints may be included in the cell from the neighbouring cells by expanding the cell size in the crossline direction as needed (typically up to 50%) to achieve a uniform coverage.
- The same midpoint could be used in more than one cell.

4.2.4.. Crossline smearing

As mentioned earlier, the centroid of the midpoints may not coincide with the centre of the cell (Fig. 14 and Fig. 15). In this case, placing the stacked traces at the centroid, rather than at the cell centre, may be considered. One problem associated with this process is that it destroys equal spacing of the stacked traces, primarily in the crossline direction. However, 3D post-stack migration, based on the Kirchhoff integral

method, may be used to produce migrated data volume with uniform trace distribution (see Yilmaz (2001)for an extended explanation about post-stack migration and Kirchhoff integral method).

4.2.5. Dip-line Versus Strike-line Shooting

The choice of the shooting direction (Fig. 16) in 3D seismic surveys is very important since, as was noted before, the crossline smearing is more severe when shooting in the strike direction.

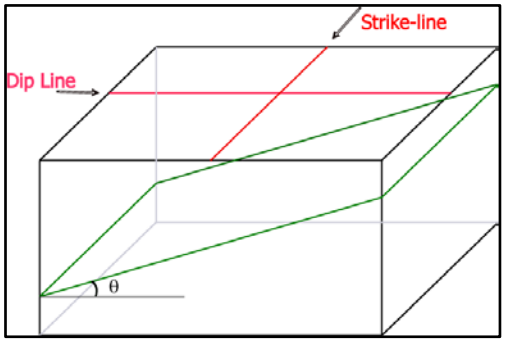

Fig. 16. Two main shooting directions: dip-line and strike-line directions (adapted from Yilmaz, 2001).

For these data acquisition, the shooting was carried out through the strike direction; nevertheless, both methods have advantages and disadvantages, which are summarized in Table 2 (adapted from Yilmaz, 2001).

Table 2. Summary of advantages and disadvantages of shooting direction.

	Dip-line shooting	***Strike-line shooting***
Advantages	Better spatial sampling in the direction of interest.	Better attenuation of coherent noise because of the moveout behaviour of side scatters.
	Possible coarser spacing reduction between lines because there is no crossline smearing.	There is not needed of DMO correction because there is not dip perceived.
Disadvantages	The complex moveout on common-cell data could cause problems in velocity analysis.	Problems with crossline smear.
	Problem of inline smear because of the reflection point dispersal along the dipping reflector associated with a non zero-offset recording.	It would require closer line spacing to prevent spatial aliasing of steep dips in the orthogonal direction.

This means that dip-line shooting must be employed almost always in data acquisition. Nevertheless, modern 3D surveys are carried out with sufficiently small inline and crossline spacing, minimizing crossline smearing and accurate implementation of 3D DMO correction for removing inline smearing.

4.3. 3D Dip-Moveout Correction

As seen previously, cable feathering in marine 3D surveys gives rise to source-receiver azimuthal variations. As a direct consequence of this acquisition-related phenomenon, stacking velocities become not only dip dependent but also azimuth dependent and must be carefully corrected. Three-dimensional dip-moveout process (3D DMO) corrects for both dip and azimuth effects on stacking velocities using the integral method applied in the time-space domain (Fig. 17). If the true dip is zero, the DMO process does not affect the data (See Yilmaz (2001) for an extended explanation of integral method and DMO correction).

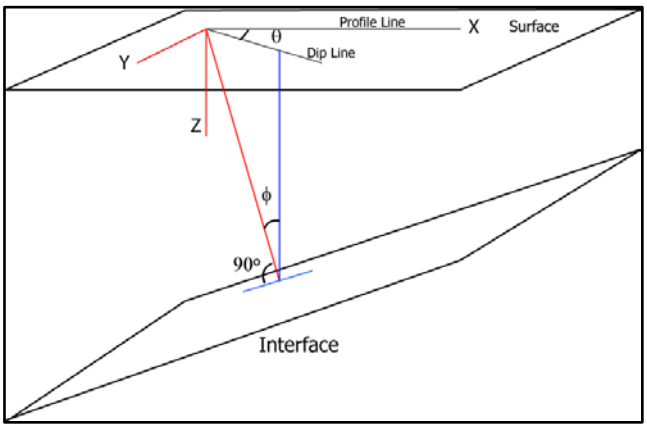

Fig. 17. Geometry for a dipping planar interface used in deriving the 3D moveout equation, where ϕ is the dip angle, and θ is the source-receiver azimuth angle measured from the dip line (Modified from Yilmaz, 2001).

4.4. 3D Velocity Analysis

For 2D data processing, a number of neighbouring CMP gathers is included in the velocity analysis to increase the signal-to-noise ratio. Similarly, when 3D velocity analysis is performed, a number of common-cell gathers are selected as 'control points'. By 3D interpolation of the velocity function between these control points, the 3D velocity field for all common-cell gathers over the entire survey can be obtained (Yilmaz, 2001).

4.5. 3D Migration

Migration is the step in seismic processing whereby reflections are moved to their correct locations in the x-y-time space of seismic data (Fig. 18), including twtt and position relative to shot points, that provides complete imaging of the 3D subsurface geology. The main benefits of migration concerns the removal of the propagation distortion from the reflectivity, the repositioning of the reflectors in their correct positions and the reduction of the amplitude of background noise without affecting the signal amplitudes (Marsset *et al.*, 1998).

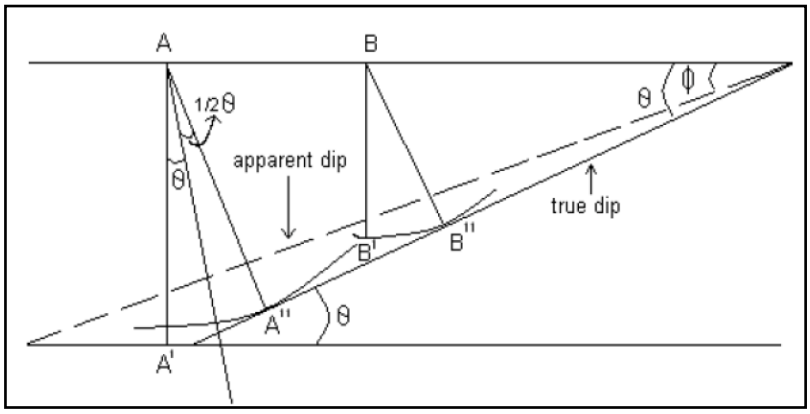

Fig. 18. Geometrical representation of migration (Kumar, 2005)

Migration processing is usually carried out after stacking (*post-stack migration*) because is less costly and involves a reduced volume of data. However, prestack migration gives more accurate results as it removes the cosine dependence of the stacking velocity on dip, forces spatial alignment and allows events of different dip at the same unmigrated time to stack correctly (Marsset *et al.*, 1998).

Efficient workflows for 3D pre-stack migration are in use today not only to image the subsurface more accurately in the presence of conflicting dips with different stacking velocities but also to generate common-reflection-points gathers that can be used to perform amplitude inversion and thus obtain attributes associated with amplitude variations with offset. 3D pre-stack time migration also paves the way for estimating a 3D rms velocity field that can be used to perform Dix conversion and thus obtain a 3D interval velocity field (Yilmaz, 2001).

Chapter 5

Interpretation of 3D Seismic Data

The acquisition and processing of reflection seismic data usually results in a seismic image of acoustic impedance interfaces. In 3D seismic exploration, this image $I(x,y,t)$ has two spatial coordinates (x,y) parallel to the surface and one perpendicular time coordinate (t) (Bakker, 2002). The time usually corresponds to the two-way travel-time (twtt).If the resulting interfaces are assumed to follow lithologic boundaries, then the seismic image is actually an image of subsurface geological units and the structures they form.

Most 3D interpretation was performed on vertical inlines and cross-lines and then projected onto a horizon slice. Also, with the volumetric image analysis we can obtain complete information about features such as faults, horizons and mounds in the earth's subsurface than slice-by-slice 2D analysis (Yilmaz, 2001).

Detailed analysis of the Miocene interval was undertaken in order to determine the existence of a proto-Ebro River within the Ebro Margin before the Messinian Salinity Crisis (MSC). Wireline logs, published stratigraphic reports (Lanaja *et al.*, 1987) and correlation to published seismic data (Bertoni and Cartwright, 2005) have been used in order to establish a correlation between the depositional and seismic units. This process allow us to establish that the Miocene unit extends over a time interval on our seismic data from about 1.27stwtt to 3.49 stwtt.

Our processed seismic data resulted in a seismic cube with horizontal grid cells of 12.5x12.5 metres and a sampling interval of 4 msec. For this study, data was sub-sampled by a factor of 2^2, resulting in seismic grid cells of 25x25 metres (see Table 3 and Table 4 to complete survey details).

Table 3. Interpreting survey details

XY Limits (Metres)	X Coordinate Range	Y Coordinate Range
	from 301264.238 to 377486.759	from 4504538.000 to 4426113.018
Record Length	3.5 sec	
Samples per Trace	876	
Sample Interval	0.004 sec	
Storage Format	8 bits	
Time Range	0 - 3.5 sec	
Projection	Universal Transverse Mercator - Zone 31	
Ellipsoid	International - 1924	
DATUM	European 1950, Mean Values	

Using the Kingdom 2d/3dPAK® Software, five horizons were identified as seismic markers. Two of them are major unconformities and were chosen as the boundaries of the interval of interest (the Top Oligocene and the Messinian Erosional Surface).Three horizons were chosen in between these major unconformities and represent clinoforms within the Miocene prograding megasequence.

5.1. Horizon Picking

Picking is usually performed on vertical seismic sections, and can form the basis for an interpreted geological section. However, and idealized geological section is rarely the final product of seismic interpretation. To arrive at a complete understanding of subsurface structures and their geology, it is usually necessary to produce maps and three-dimensional models of the subsurface. This necessitates the interpretation and picking of multiple seismic sections in a survey area. The availability of a 3D image volume facilitates better interpretations, even for inherently two-dimensional structures (Yilmaz, 2001).

Conventional seismic interpretation consists of mapping geologic structures of the studied area. After inspection and preliminary interpretation, the next step in interpreting seismic images is reflector *picking* and *tracking*. *Picking* involves identifying and recording the position of specific reflection events, while *tracking* implies to follow this reflector over the seismic image (Bakker, 2002).

The main reflection events to identify are the *horizons*, which are surfaces that separate different rock layers in depositional environments characterized by different reflection properties (Bakker, 2002). Some of these surfaces are selected and followed by the interpreter over the volume. There are several reasons why a reflector is selected as horizon. The main one is that appears outstandingly clear and strong, making it easy to track. Also sequence boundaries are important horizons to distinguish between the different geological periods (Avseth *et al.*, 2005).

There exist various techniques for horizon picking: manual, interpolation, autotracking, voxel tracking, and surface slicing (see Dorn (1998) for detailed descriptions). Three-dimensional horizon picking is a difficult, more complex and more computationally demanding task. Some algorithms have recently been developed for 3D *autopicking*, detecting horizons as the union of small 3D seismic surfaces or model them as triangulated surfaces. The obvious advantage of *auto- picking* or *-tracking* is the speed and efficiency; however, a lateral change in polarity or a fault within an event could not be recognized because this technique assumes that seismic horizons are locally continuous and consistent (Avseth *et al.*, 2005). Also, in areas of low S/N, the autopicking may fail to track the correct horizon.

After data sub-sampling, our 3D seismic survey results in 1888 inlines and 2511 crosslines, which were picked every 40 increments(Table 4) using the Kingdom 2d/3dPAK® Software for geophysical interpretation, which allows to generate horizons and faults in both time and depth domains and to produce seismic-based interpretation maps by combined utilization of horizon and fault picking tools.

Table 4. 3D seismic data details

Initial details		**Min. Value**	**Max. Value**	**Increment**	**Spacing (m)**	**Count**
	Inline	1036	4810	2	24.9938	1888
	Crossline	1840	6860	2	24.9959	2511
Picking details		**Min. Value**	**Max Value**	**Increment**	**Spacing**	**Count**
	Inline	1036	4796	40	500	95
	Crossline	1858	6858	40	500	125

The picking process was carried out using the *Autopick - Fill* mode over the *peak* event. The *peak* data type event fits a parabola to three samples near the peak and its time and amplitude are computed from the parabolic fit. The *Autopick - Fill* tool picks points between single clicks with the event dropped to the appropriate phase while honouring the guide window in only one direction. This feature performs even when the current traces do not contain any prior horizon seed picks (Seismic Micro-Technology, Inc., 2008).

Five horizons were selected within the time interval of interest and followed all over the inline and cross-line sections. For that, horizons were picked on an inline/cross-line and followed along it as far as possible, intersecting with other cross-lines/inlines where the picks can be transferred. By working round a loop of lines, it is possible to get back to the starting point, where it can be checked that the interpretation was consistent around the loop (Bakker, 2002). Because their discontinuity in some areas, seismic correlation of these horizons was started in the more continued sections and then connected to the slope areas, where correlation was more challenging. The result was a mesh composed of cells of 500x500 metres (Table 4; Fig. 19).

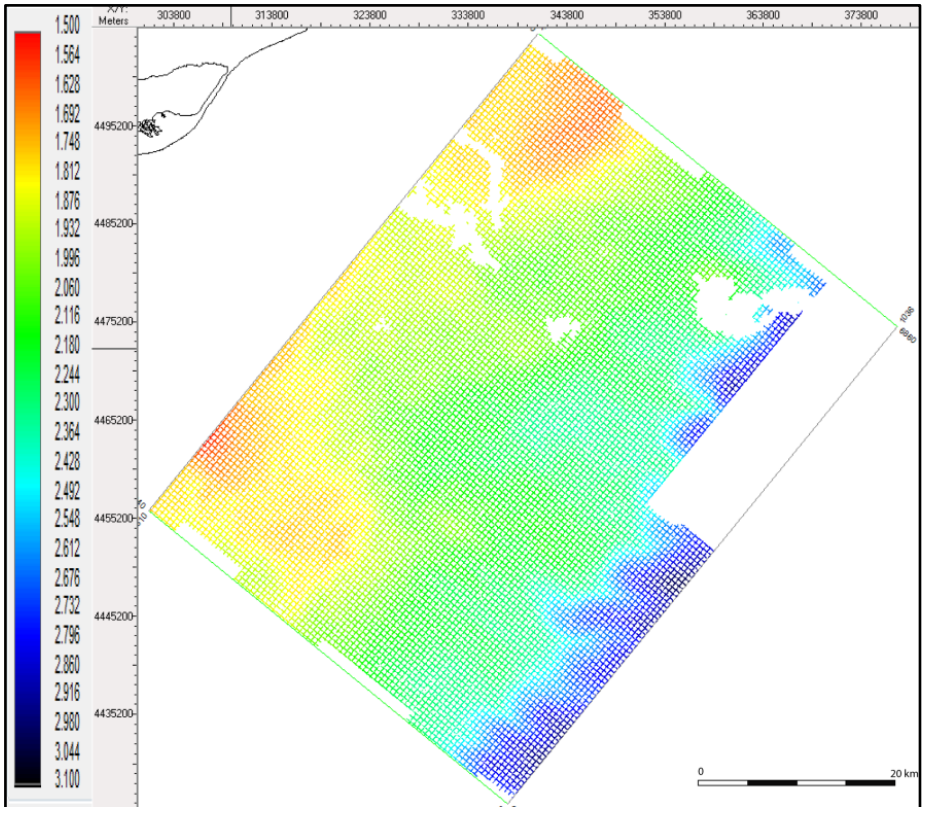

Fig. 19. Mesh density resulted from PreMess1 horizon picking every 20 lines along inline and crossline directions (colour scale is in stwtt seconds).

Since tracking a horizon across a 3D survey, which contains hundreds of inlines and crosslines, is time consuming, to complete the area tracking we used *Digitize a Polygon Hunt* tool to infill interpretation on the obtained meshes. The result is the extension of the picked horizons across the entire survey area (in-lines and crosslines).

5.2. Extracting Isobath Maps

From the obtained surfaces, we extracted isobath maps by computing a contour (Table 5) that link the picked points of the same time belonging to the same horizon.

Table 5. Contour parameters used to obtain isobath maps

Contour Interval	0.1 sec
Minimum Contour Value	1.6 sec
Maximum Contour Value	3.5 sec
Sample Increment in Bins	1
Max. Projection Distance Multiplier	Infinite Bin
Detailed Threshold Size	152.4 m

This maps represents the morphology of an interpreter horizon, i.e. the equivalent of a topographic map of each surface. They give an idea of the slope and the main dip direction of these surfaces.

5.3. Calculating Composite Surfaces and Isochore Maps

Isochoric maps display the variation of volume within a stratigraphic unit, providing information about the amount of sediment deposited in the area during a certain time interval, and therefore, about the movement of the depocentres.

Due to spatial distribution of the horizons selected for picking, before extracting isochoric maps is necessary to perform a series of composite surfaces (Fig. 20). This composition consisted of the application of a mathematical operation (OR [when both horizons have data, choose the first; where only one has data, choose the horizon; where neither has data, choose null]) where the data of the isochron of interest were selected in order to establish the upper and lower sedimentation boundaries of the units (Table 6).

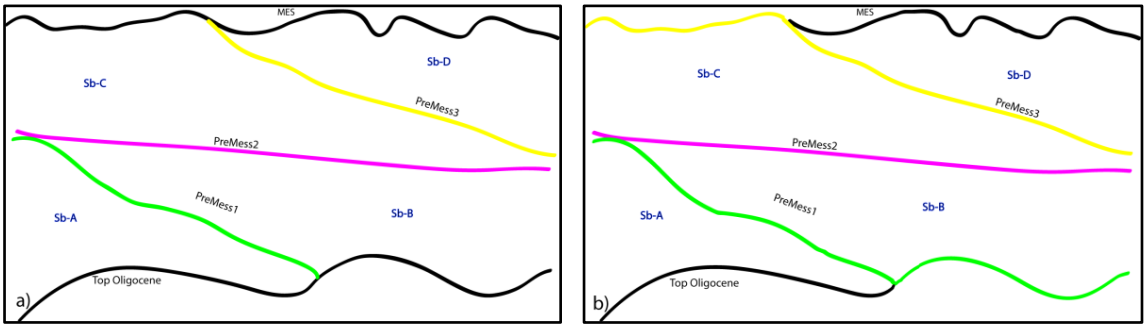

Fig. 20. a) Scheme of picked horizons(in black) showed in dip direction and the four subunits (in blue)generated within this interval; b) Scheme of composite applied to PreMess1||Top Oligocene and to PreMess3||MES.

The resulting composite surfaces are the following (Fig. 20):

- PreMess1 || Top Oligocene, to establish the lower boundary of unit Sb-B.
- PreMess3 || MES, to establish the upper boundary of unit Sb-D.

Table 6. Thickness maps obtained and boundaries used for the operation.

Sedimentary Unit	**Lower limit**	**Upper limit**
Sb-A	Top Oligocene	PreMess1
Sb-B	PreMess1||Top Oligocene	PreMess2
Sb-C	PreMess2	PreMess3||MES
Sb-D	PreMess3	MES
Top Oligocene-PreMess2	Top Oligocene	PreMess2
Top Oligocene-PreMess3	Top Oligocene	PreMess3||MES
Miocene thickness	Top Oligocene	MES

Having established the upper and lower boundaries of each unit of interest (Table 6), isochoric maps were extracted by basic mathematical subtraction, obtaining the difference of depth between both limits, which is equivalent to the thickness of sediments deposited between the two surfaces.

Chapter 6

Seismic Attributes

Seismic attributes were introduced in the early 1970's and have become an integral part of seismic interpretation projects. They are defined as *"all the information obtained from seismic data, either by direct measurements or by logical or experience-based reasoning"* (Taner, 2001). The principal objectives of the attributes are to provide accurate and detailed information to the interpreter on structural, stratigraphic and lithological parameters of the study area. The idea is to use such techniques to establish shapes or appearances of anomalous entities seen in the data and then to discuss their geological implications (Chopra and Marfurt, 2007).

There are more than 50 seismic attributes applied to the interpretation of geologic structure, stratigraphy, and rock/pore fluid properties, revealing 3D geologic patterns that had been impossible to discover from geometric interpretation of the wiggle traces in 2D stack sections (Chopra and Marfurt, 2007).

Attributes are defined by a value and a position in 3D space (inline, cross-line and Z (twtt or depth)), and can be calculated from single-trace, multi-trace and multi-volume inputs (dGB Beheer B.V, 2009). All seismically-driven parameters can be defined as seismic attributes. They can be velocity, amplitude, frequency and the rate of change of any of these with respect to time or space (Taner, 2001).

Attributes can be classified in many different ways. Here we give a classification based on the computational characteristics (Taner, 2001):

- *Geometrical Attributes*: They describe the spatial and temporal relationship of all other attributes. They are used for stratigraphic interpretation, quantifying features that directly assist in the recognition of depositional patterns and related lithology.

- *Physical Attributes*: Those attributes related to physical qualities and quantities of seismic data. They provide us with information on reflector amplitude, waveform and variations with illumination angle and are mostly used for lithological classification and reservoir characterization.

Today's computers are able to compute 3D seismic attributes over an entire data volume, creating attribute volumes. Because each point in the attribute volume is computed using a 3D neighbourhood, the detection of geological features is less dependent on the exact location, and therefore less dependent on carefully picked horizons (Bakker, 2002).

6.1. Seismic Amplitude

About 30 years ago, Taner and Sheriff (1977) introduced the concept of using the Hilbert's Transform to calculate simple seismic attributes instantaneously, meaning a value for each parameter is calculated at each time sample of a seismic trace (See Taner and Sheriff (1977) for an extended explanation). This simple attribute represents the contrast in elastic properties between individual layers.

The quantitative interpretation of amplitudes can add information about stratigraphic features (e.g., channel systems), lithology, porosity, fluid accumulation, as well as pore-pressure. Conventional amplitudes are useful for viewing faults that run perpendicular to strike; however, when faults run parallel to strike, they become difficult to interpret as fault lineaments. Similarly, small or minor faults are not so evident on the seismic data volumes since they have a minute reflector offset (Chopra and Marfurt; 2007).

6.1.1. Calculation Process Description

In this work, amplitude maps of each picked horizon were extracted in order to investigate the sedimentary features that could potentially give clues on the existence of a proto-Ebro river before the MSC. To extract the amplitude attribute, we used the *Volume Attribute Calculator* included into Kingdom 2d/3dPAK® Software, which allow us to calculate the amplitude from an interval of the seismic traces.

We have extracted the amplitude comprised in between 0.05stwtt below and 0.05stwtt above each horizon. It was calculated by four different mathematical operations (Table 7).The most consistent results were obtained with extraction of the most negative amplitudes.

Table 7. Methods used for amplitude map calculation

Extracted Amplitude	**Calculation**
Amin	The largest negative amplitudes are stored
Amax	The largest positive amplitudes are stored
Amean	The mean amplitudes of the interval are stored
Arms	The root-mean-squared of the amplitudes are stored

6.2. Seismic Coherency

Routine acquisition of 3D, high-quality seismic data, and its eventual interactive interpretation on workstations, has helped immensely in resolving faults and fractures. However, picking fault surfaces is time consuming, since they need to be marked on inlines and crosslines and then combined into fault surfaces. Moreover, small faults may have a minute reflector offset, in most cases appearing as an inconsequential disruption, making them difficult to directly detect (Chopra and Marfurt, 2007).

Coherence technology has provided interpreters a new way of visualizing faults and stratigraphic features in 3D seismic data volumes. This seismic attribute was developed in the mid-1990s as a group of algorithms that measure the trace-to-trace similarity of the seismic waveform within a small analysis window (dGB Beheer B.V, 2009). Discontinuities in the layered structure of sedimentary rock are shown as discontinuities in reflection continuity, highlighting faults and stratigraphic features such as reefs, channel boundaries or deltaic sediments.

And attractive characteristic of the coherence attribute is that it gives an unbiased view of the features in the seismic volume because not-interpretation is required. Moreover, since the three-dimensionality is an essential ingredient of coherence computation, faults or fractures in any orientation are revealed equally well, solving the problem associated to the amplitude attribute (Chopra and Marfurt, 2007).

6.2.1. Calculation Process Description

For each point in a 3D seismic volume, it shifts one of the traces up and down to find the maximum cross-correlation and awards a value between 0 (not similar at all) to 1 (completely similar).The coherence is measured twice, between the current position represented by the vector X and the following two vectors: Y (is the vector in the same inline, but on the next crossline) and Z (is the vector on the same crossline, but on the next inline) (dGB Beheer B.V, 2009).

For this survey, coherence maps of each studied horizon were extracted in order to investigate the imprint of features that reveal the sedimentary dynamics of the margin and potential imprint of a paleo-Ebro River's before the MSC. To extract the coherence attribute maps, we used the *Volume Attribute Calculator* included into Kingdom 2d/3dPAK® Software. This calculation was performed all along an established time-window, which covers 0.05 stwtt below and 0.05 stwtt above the horizon of interest. The outputs corresponding to this interval were calculated using four different mathematical operations (Table 8):

Table 8. Calculation methods used for obtaining coherence maps.

Extracted Coherence	**Calculation**
Cmin	The largest negative coherence are stored
Cmax	The largest positive coherence are stored
Cmean	The means of the coherence are stored
Crms	The root-mean-squared of the coherence are stored

Chapter 7

Results

Seismic survey of the Ebro Margin extends between 0 and 3.5 stwtt (Fig. 21), corresponding to the acoustic basement and the seafloor, respectively. Within this interval, two megasequences separated by an erosional surface are recognized. Due to the acquisition geometry, crosslines are almost perpendicular to the margin strike while inline sections are parallel to the margin strike.

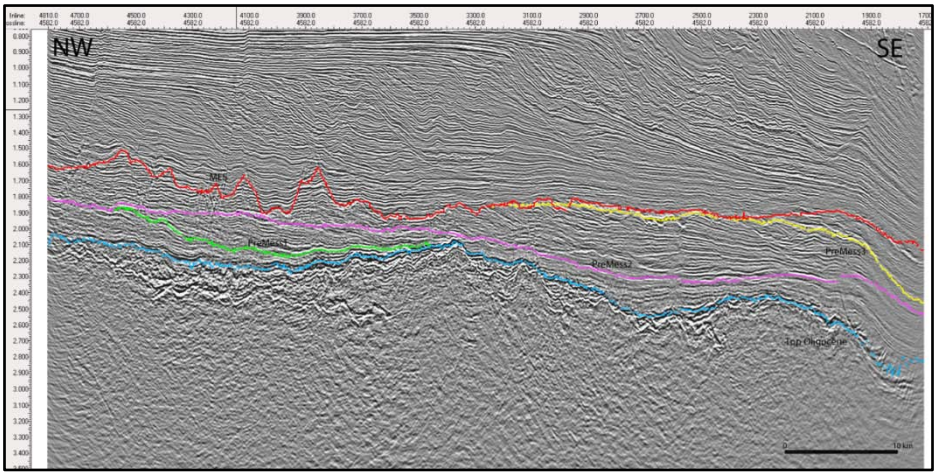

Fig. 21. Crossline 4582.0 in the studied area. The sequence illustrates the Miocene unit, between the MES (red) and the Top Oligocene (blue). The interior solid lines (PreMess1 (green), PreMess2 (pink) and PreMess3 (yellow)) refer to the three horizon mapped in the studied area.

Our study comprises the interval from the end of the Oligocene (about 23 Mya) and the Messinian Salinity Crisis (5.6-5.33 Mya), which marked the end of the Miocene Epoch. In the 3D seismic record, this sequence is enclosed between 1.22 and 3.49 stwtt, with a maximum thickness of 1.1 stwtt.

The Miocene sequence is characterized by simple sigmoidal clinoforms exhibiting a mainly progradational geometry and a gentle seaward shift in the offlap break position (Fig. 21, Fig. 23 and Fig. 24). This interval includes the Megasequence identified as Castellon Group by Frey-Martinez *et al.* (2004) and Bertoni and Cartwright (2005).

Internal reflectors display wedge-shaped geometries, dipping basinwards and with a predominant prograding character. Within this interval, four different acoustic facies are recognized (Fig. 22):

- *Stratified facies*, characterized by parallel reflectors.
- *Chaotic facies*, characterized by discontinuous and randomly oriented reflectors.
- *Transparent facies*, with poor defined or absent reflectors.
- *Wavy facies*, characterized by moderate- to high- amplitude seismic undulating reflections.

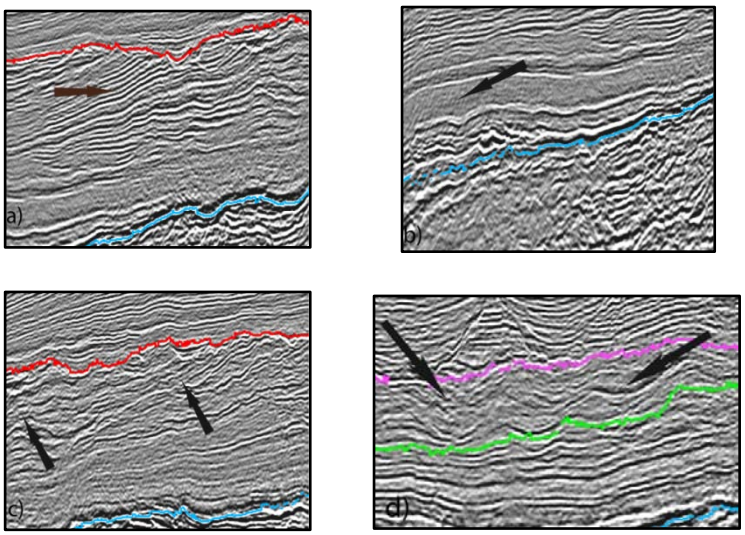

Fig. 22. Examples for seismic facies recognized in the studied area. a) Parallel facies; b) Transparent facies; c) Chaotic facies; d) Wavy facies.

7.1. Seismic Geomorphology

The Miocene depositional package is bounded by two regionally extensive surfaces that represent transformations in the architectural style of the margin: the Top Oligocene at the bottom and the Messinian Erosional Surface (MES) at the top. Within this interval, three mapped seismic reflectors, named PreMess1, PreMess2 and PreMess3 (from oldest to youngest),were picked all over the survey area in order to define geomorphology of the Ebro Margin at the time of deposition of reflection generating strata, and place them in a seismic-stratigraphic framework. It is emphasized that horizon definition was not based on standard sequence-stratigraphic criteria, but rather by the need to establish accurate seismic stratigraphic markers for the mapped area as a whole.

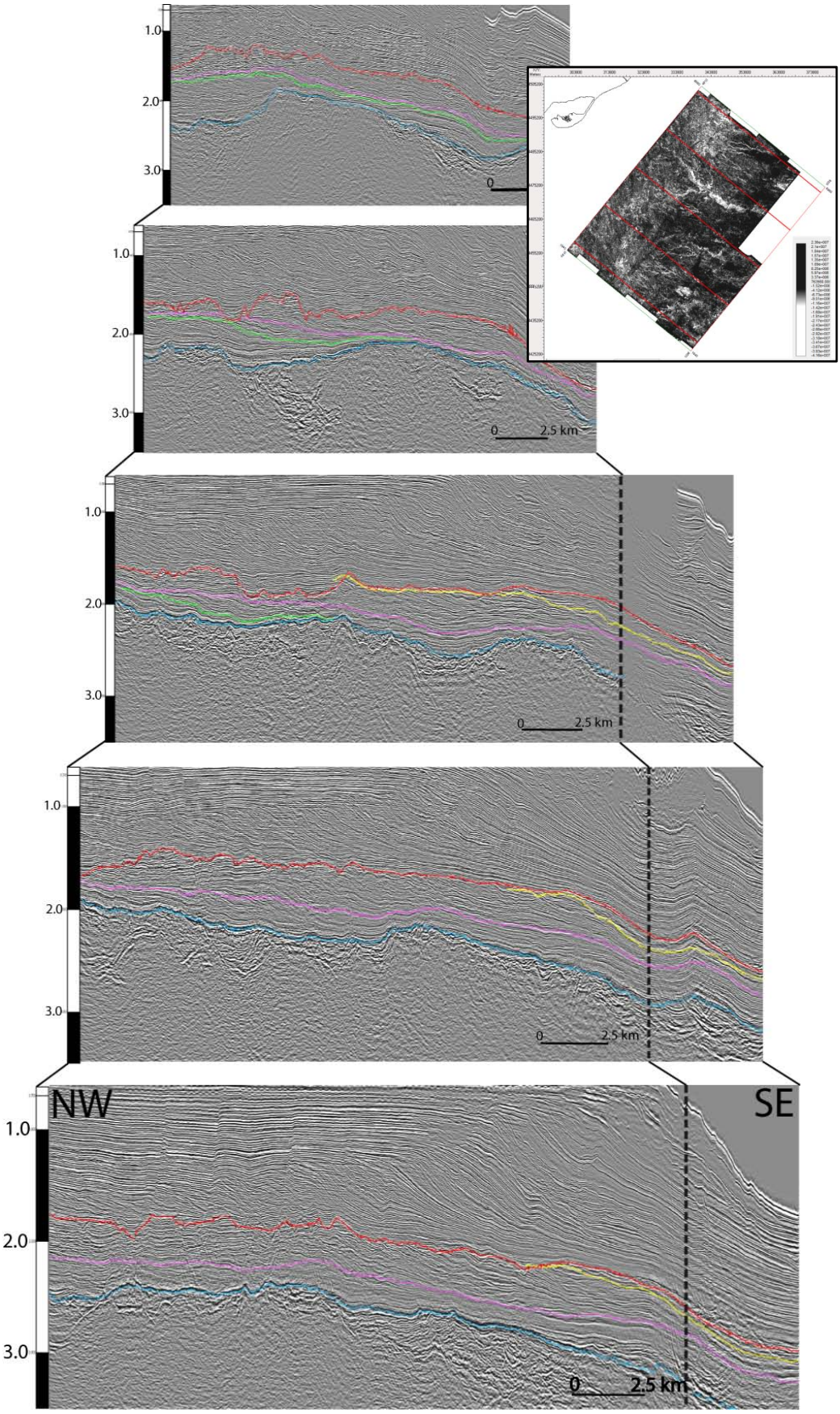

Fig. 23. Seismic profiles along the dip direction, perpendicular to the shoreline (crosslines 2098, 3248, 4398 and 6698, from NE to SW and from up to down) showing the geometry of the intra-Miocene horizons. (In miniature, base map displaying crosslines location).

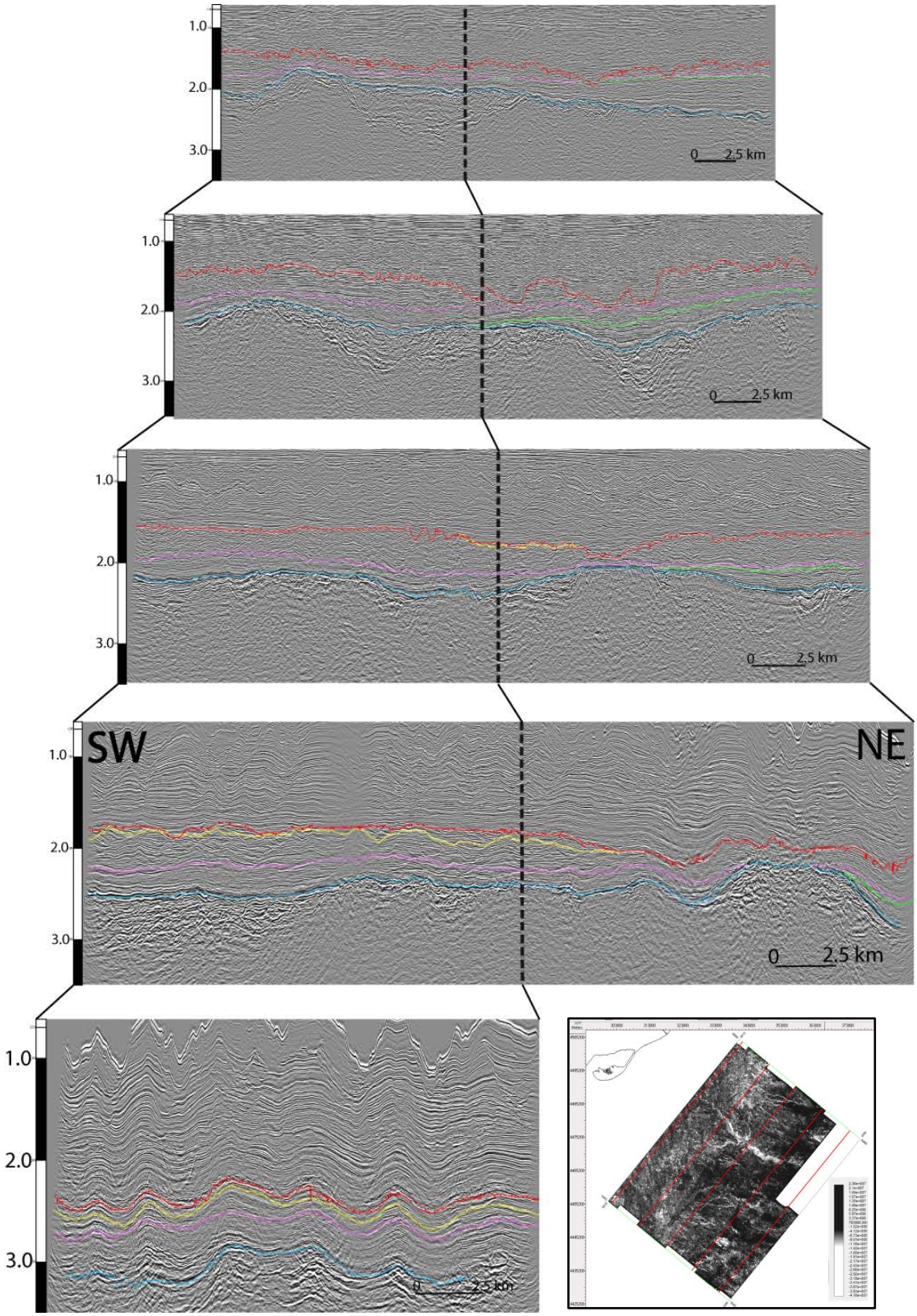

Fig. 24. Seismic profiles along the strike direction, parallel to the shoreline (inlines 4716, 3876, 3036, 2196 and 1356, from NW to SE and from up to down) showing the geometry of the intra-Miocene horizons. (In miniature, base map displaying crosslines location).

7.1.1. Top Oligocene

This horizon, which constitutes the Miocene base is recognized across the entire survey by a strong irregular seismic reflection placed between 1.61 and 3.49 stwtt (Fig. 23and Fig. 24).The horizon is characterized by a slight northwest-southeastern dipping direction, as can be seen along the crosslines and inlines (Fig. 23 and Fig. 24), and a major break-of-slope perpendicular to it (northeastern-southwestern direction) located 70 km offshore from the present-day coastline.

Broadly, the general structure is a NNW-SSE high-and-low succession: 1) depression axis; 2) structural high; 3) depression axis; 4) structural high; 5) depression axis (Fig. 25), generating by a series of ENE-WSW normal faults responsible for the horst-and-graben structure. This morphology is greatly consequence of the main rifting phase that affected the Mesozoic/Paleozoic Basement during the Oligocene (Dañobeitia *et al.*, 1990; Escutia and Maldonado, 1992).This morphology will be key in depocentre evolution during the Miocene.

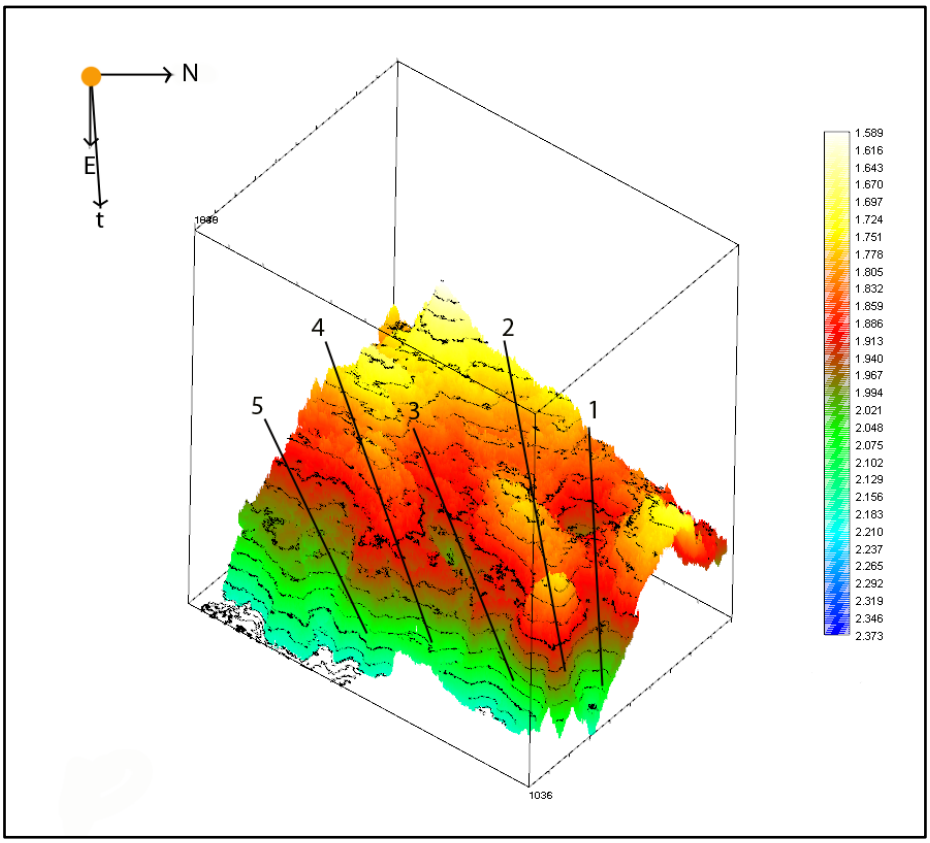

Fig. 25. 3D view of the Top Oligocene horizon. The general structure is characterized by a high-and-low succession: 1) depression axis; 2) structural high; 3) depression axis; 4) structural high; 5) depression axis (colour scale is in stwtt units)

The amplitude map (Fig. 40, Appendix A) displays the nature of troughs (sedimented areas) and highs (Paleozoic/Mesozoic basement), respectively displaying positive (black) and negative values (white). In the southwest part of the studied area, a series of northeast-southwest alignments are highlighted both in the amplitude and coherence maps (Fig. 26, Appendix A). This banded area corresponds to a series of listric normal faults dipping to the southeast, some of which appear even cutting to PreMess2 horizon.

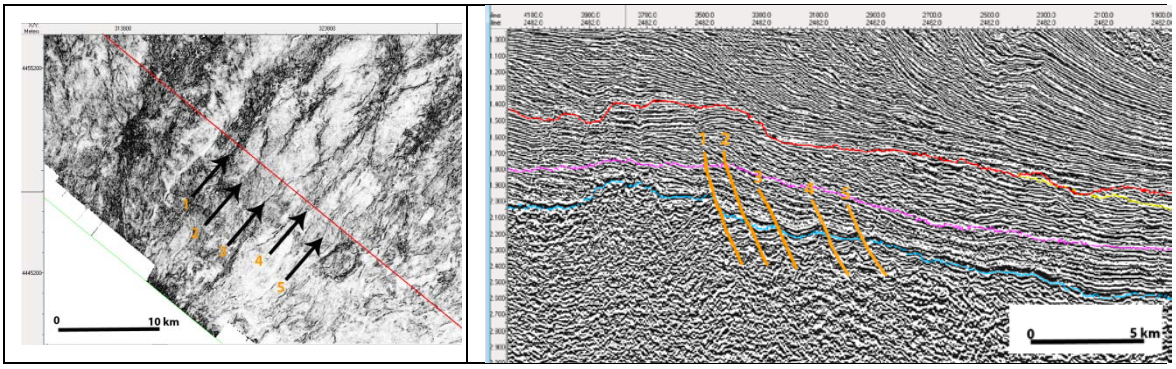

Fig. 26. a) Map detail of Top Oligocene's coherence with identification of fault alignment (close to zero coherence values); b) Interpretation of mentioned faults throughout a crossline 2482 fragment.

The coherence map of Top Oligocene shows the same northeast-southeast alignments observed in the amplitude map as well as other fault systems all along the survey area (Fig. 41, Appendix A)

7.1.2. Messinian Surface

The Messinian Erosional Surface (MES) constitutes the top of our study interval and is recognized all along the survey area at depths between 1.22 and 2.82 stwtt as an unconformity (Fig. 21 and Fig. 27). In some areas, this erosional event appears truncating Subunits C and D (Sb-C and Sb-D) in topsets and foreset (Fig. 31).

Time structural map displays two topographic highs bisected by a major NW-SE oriented valley, characterized by a complex and laterally high variable geometry. This horizon presents three major morphological regions arranged roughly parallel to the present coastline (Fig. 27). These regions are bounded by two clearly recognizable steps located about 50 and 70 km seaward from the present-day coastline From proximal to distal areas, the MES morphology displays: a flat-steep (Region 1), a flat (Region 2)

and a steep (Region 3), profile in a similar way to that reported by Urgeles *et al.* (2010) for this area (Fig. 27).

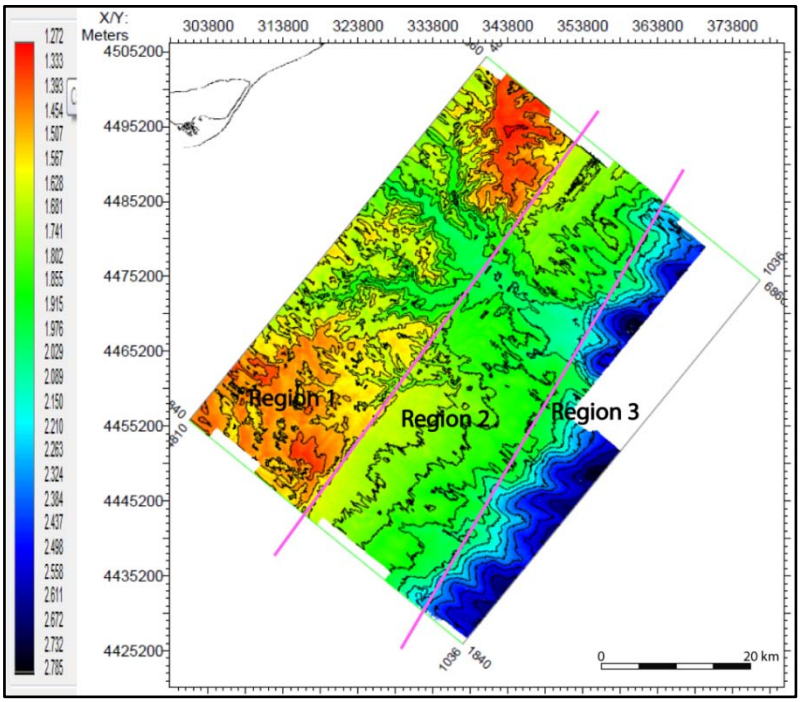

Fig. 27. Messinian Erosional Surface isobath map showing the two main steps located 50 and 70 km away from the coastline (colour scale is in stwt units).

- *Region 1*: It is the most proximal region. On its northwestern sector it presents a highly rugged relief with an intricate drainage network. Most identified streams within this region coalesce in the main valley. The major contribution to the Messinian relief results from erosional processes, which gave rise to a morphology that some authors have defined as suggestive of 'bandland topography' (Frey-Martinez *et al.*, 2004).
- *Region 2*: It is an area of relative low and smooth relief dipping gently to the SE. On the time-structure map (Fig. 27) the only incisions that can be seen to cut to through that region are major valleys. The limit between Regions 1 and 2 is rather steep and rectilinear, but seismic data does not suggest tectonic control on that boundary.
- *Region 3*: Time structural map suggest a third region in the southwestern most distal fringe of the 3D seismic survey. This region dips smoothly basinward.

While time-structure map only reveals the major drainage systems, amplitude map displays a complex detritic system of canyons and channels (Fig. 28). The main Messinian valley cuts the topset of the Castellon Group and continues incision along the foreset. This major valley shows a channel with well-developed meanders characterized by minimum amplitude values. The length, drainage pattern and channel characteristics of this major valley recorded on the MES are only comparable with the valleys carved by the large Mediterranean rivers during the MSC (Rizzini *et al.*, 1978; Clauzon *et al.*, 1982). Since this major valley expends from a similar position to the present Ebro River, it seems logical to think that it is the Messinian Ebro River valley, agreeing with Roger *et al.* (2010).

Also, the map shows that the three regions identified in the isochron map have slightly different minimum amplitude data. *Region 1*is arranged parallel to the coastline and presents lower minimum amplitude values. Most valleys that appear in that region have low minimum amplitudes. *Region 2* is bounded by the two breaks-of-slopes displayed in Fig. 27 and Fig. 28. Most of the minor drainage systems are placed in this region and begin along the major slope-break in the form of a branched head region merging progressively into a single axis downstream (Fig. 28.a, b). The maximum width of major channel occurs into it. In *Region 3*, most of the drainage systems disappear or their boundaries appear more diffuse.

The steeped character of the MES is evocative of a sea cliff and a marine abrasion platform (Fig. 27), with a scarp over most of the boundary between Regions 1 and 2, and a platform at its foot (Region 2). The little erosion created by the streams observed in this first boundary suggests predominance of transport/deposition processes or emergence of this region for a relative short time period. A probably Messinian stable base level appears to occur at the most distal scarp (between Regions 2 and 3), where most of the streams vanish. This seems be in agreement with the fact that the Messinian Ebro River presents a flat bottom valley, low gradient and meandering nature.

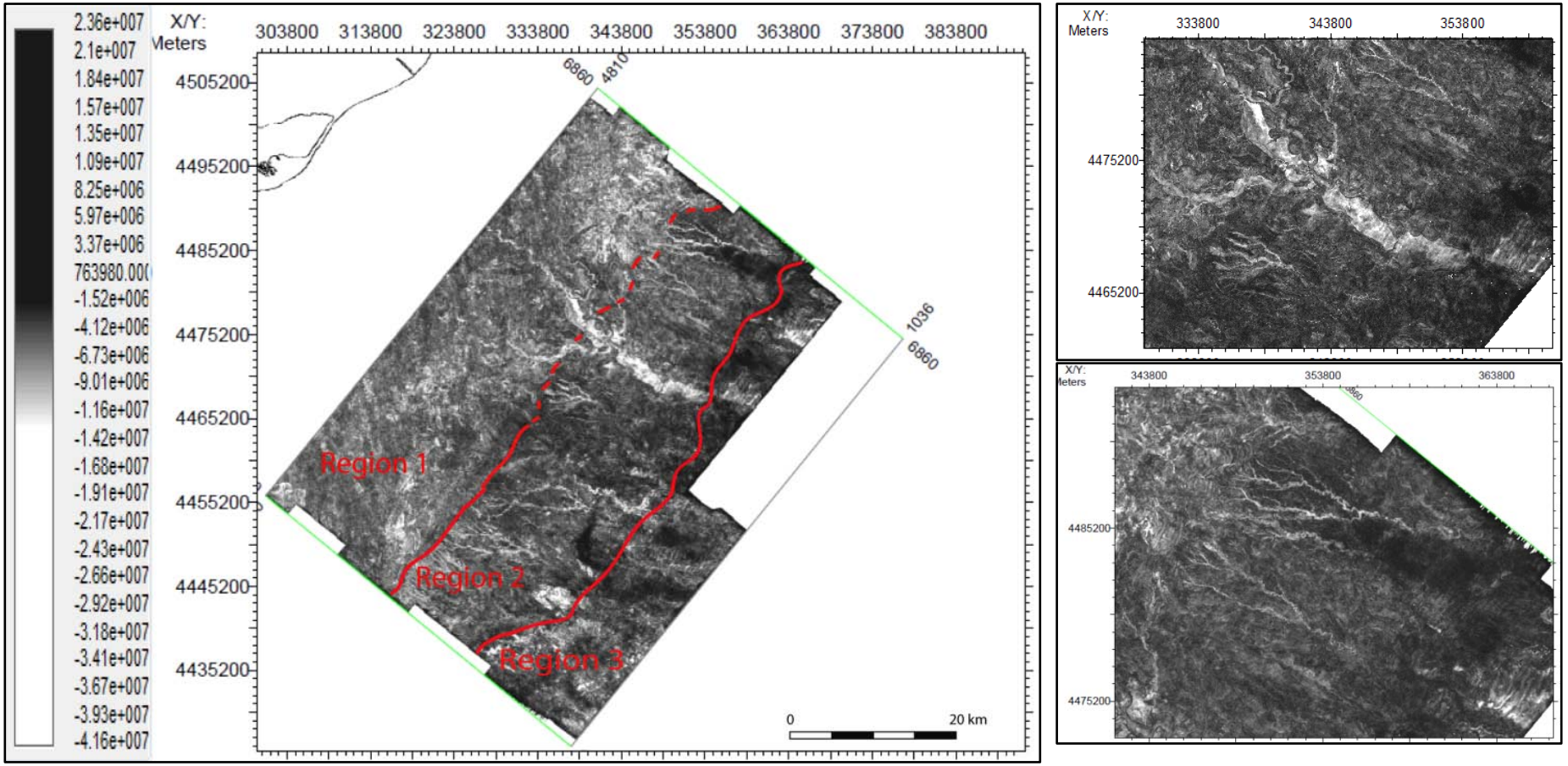

Fig. 28. a) Amplitudes map for the Messinian Surface. A clear main drainage network is observed, as well as some secondary channels. Three main regions according to amplitude values have been delimited; b) Detail of main valley; c) Zoom showing two secondary channel networks.

The Messinian coherence map (Fig. 29) displays also the features identified in the MES amplitude map, including meanders and the three main regions previously seen in time-structure map.

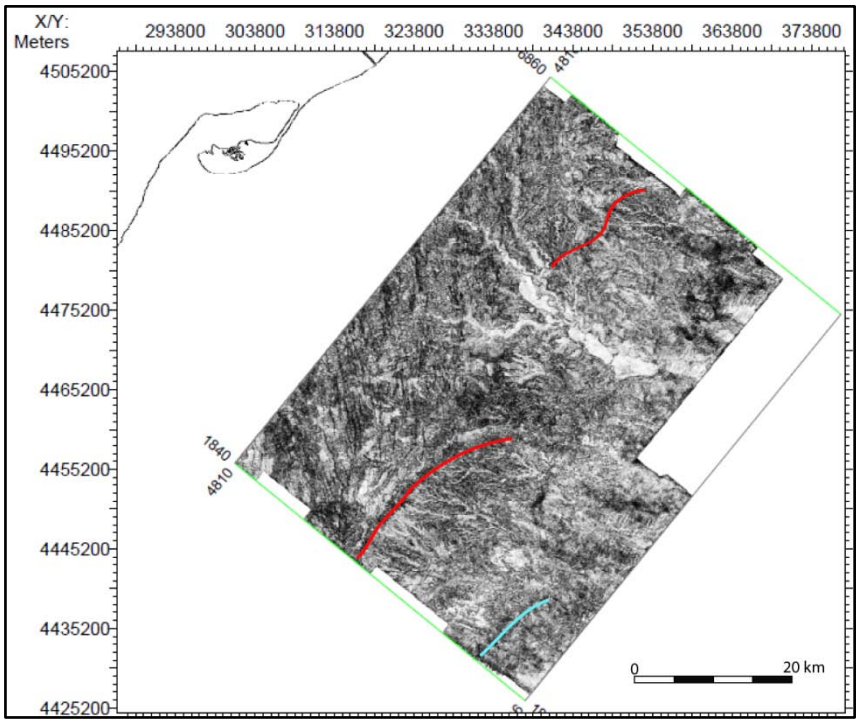

Fig. 29. Coherence data map for the Messinian Erosional Surface showing the drainage network. Primary and secondary breaks-of-slope, characterized by low coherence values are marked (red and light blue, respectively). Dark colours indicate lower coherency, lighter colours indicate higher coherency.

A system of roughly north-south fault is imaged on this horizon along the western part of the survey area (Fig. 30).These faults can be observed in the corresponding inlines

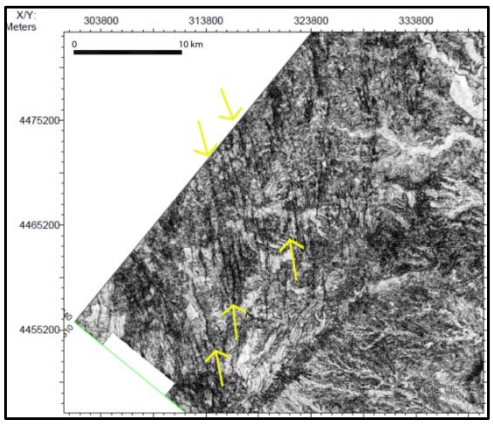

Fig. 30. Detail of coherence map indicating the fault alignment situated in the northeastern part of the survey area.

7.1.3. Clinoforms within the Miocene Interval

Three intra-Miocene reflectors between Top Oligocene and the MES interval were picked in order to establish the sediment distribution patterns within this interval. The reflections are characterized by simple sigmoidal clinoforms exhibiting a mainly progradational geometry and a gentle seaward shift in the offlap break position (Fig. 23 and Fig. 24). All of them are deeply cut by the valley and the complex detritic network of tributaries developed during the Messinian Salinity Crisis, making the erosional and sedimentary study of these horizons more difficult (Fig. 31).

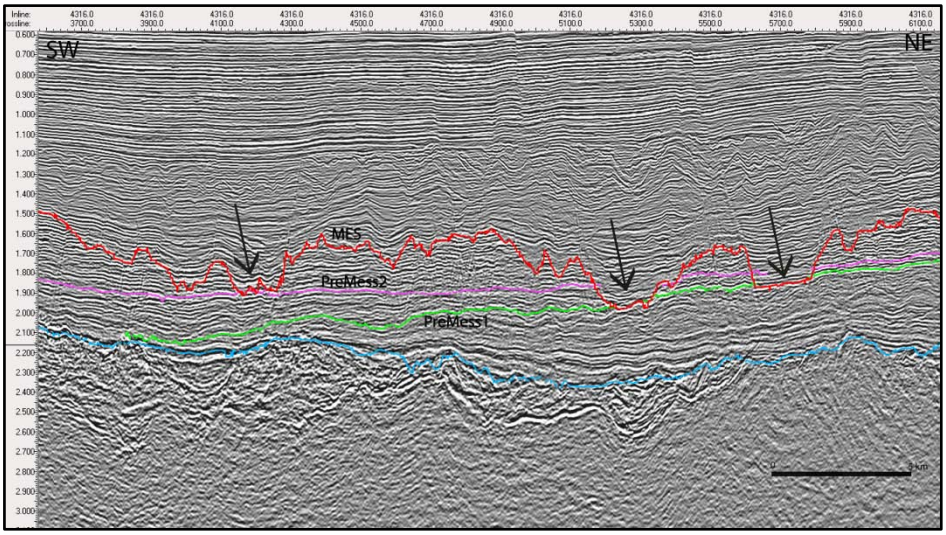

Fig. 31. Seismic Inline 4316 showing erosional truncation of PreMess1 (green) and PreMess2 (pink) horizons by the MES (red).

7.1.3.1. PreMess1

The oldest intra-Miocene surface, PreMess1, is confined to the northern part of the study area at depths between 1.65 and 2.74 stwtt. It displays a morphology that mics relatively well the acoustic basement, clearly dipping towards the southeast. Overall its shallower in the northern sector of the survey area. A slope-break, quite parallel to the coastline, is distinguishing about 60 km away from the coast (Fig. 42, Appendix A)

The seismic interval bounded by the Top Oligocene and the PreMess1 has been denoted as Subunit-A (Sb-A) and displays a lobe structure of which we probably only image the western half. In those zones coinciding with the troughs, two different seismic facies were found (Fig. 32). In the deeper part of the package, bounding with the Top Oligocene, acoustic facies are subparallel, exclusively filling the troughs. The

upper package section results in oblique clinoformal morphology with well-developed toplap geometry.

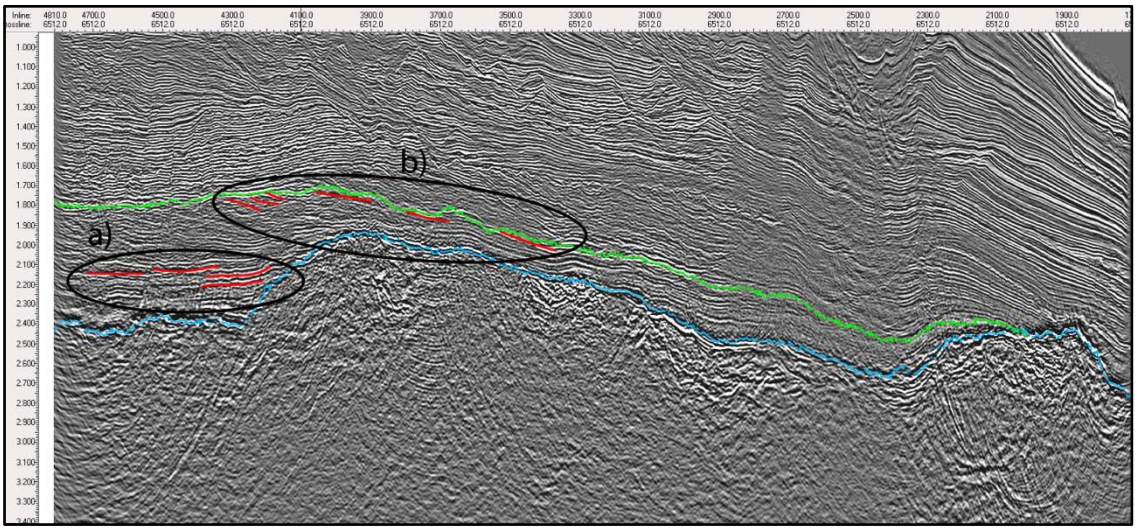

Fig. 32. Interpretation of PreMess1 morphology and types of seismic facies within Sb-A Crossline 6512. a) Seismic facies are subparallel and fill the trough associated to the rifting period; b) Truncation of reflectors against PreMess1.

Seismic amplitude data for PreMess1 shows the northwestern region elevated with respect to adjacent areas and parallel to the coastline, with lower amplitude values. Seaward, the horizon displays a banded pattern with medium and high amplitude values in the dip-line direction, ending with the highest values in the deepest part of the horizon (Fig. 43, Appendix A). Amplitude variations along the dip probably correspond to submarine channels and sediment pathways.

Two wide areas with lower coherence values are recognized for the PreMess1 (Fig. 44, Appendix A), which correspond in the seismic profile with wavy seismic facies (Fig. 33). There is a correspondence between these low coherence areas and the banded areas located on the amplitude map.

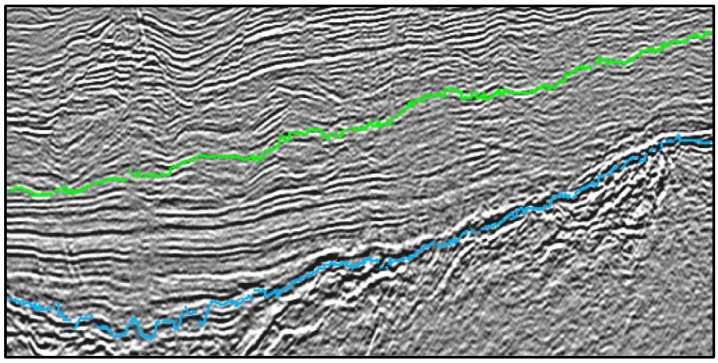

Fig. 33. Detail of Line 4018 where wavy morphology of the horizon is appreciated.

7.1.3.2. PreMess2

The PreMess2 surface lies between 1.57 and 3.03 stwtt covering the entire survey area(Fig. 45, Appendix A).The time structural map displays two elevated areas separated by a deep and wide topographic low trending northwest-southeast, characterized by a complex and laterally high variable geometry. The slope-break is placed about 65 km seaward from the coastline.

This seismic interval (Sb-B) is generally characterized by southeast dipping sigmoidal clinoforms. It displays continuous and laterally persistent reflectors, both along strike and dip directions (Fig. 34). In some zones, the package is eroded by the Messinian Erosional Surface, removing a large portion of the sedimentary succession (Fig. 31).

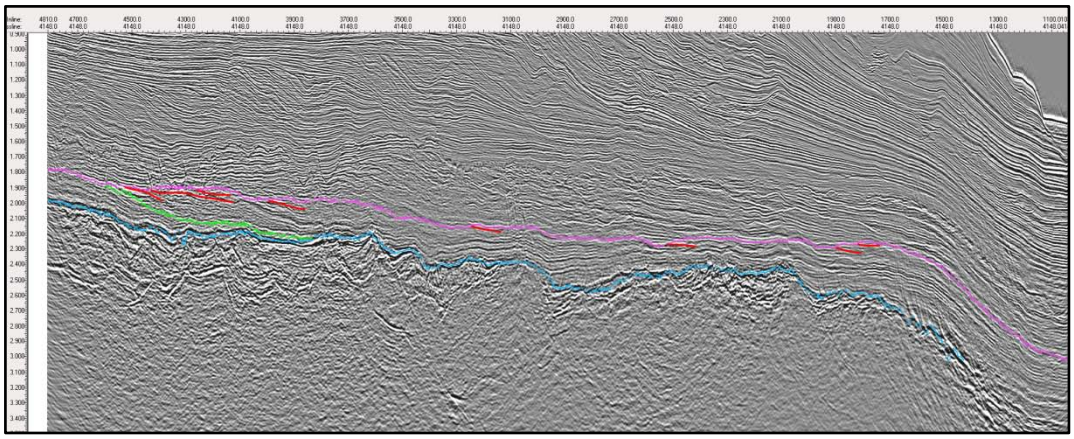

Fig. 34. Crossline 4148 showing sigmoidal shape of the reflectors.

Amplitude data reveal three regions with different amplitude ranges (Fig. 46, Appendix A), similarly to the MES. A first region, with lower values (light colours), situated between the coastline and the first slope-break. In some regions the seismic package is eroded by the MES. This is recorded in the amplitude map due to the volume calculation method, as explained in the previous sections. The second region corresponds to the area bounded by the two major changes in slope, showing a banded morphology with middle to high amplitude values, which extends in the dip direction. As in PreMess1, these banded areas coincide with wavy reflectors. The third region displays the highest amplitude values, extending from the major slope-break to the end of the survey area. Some subtle channels can be located in this region (Fig. 35.a).

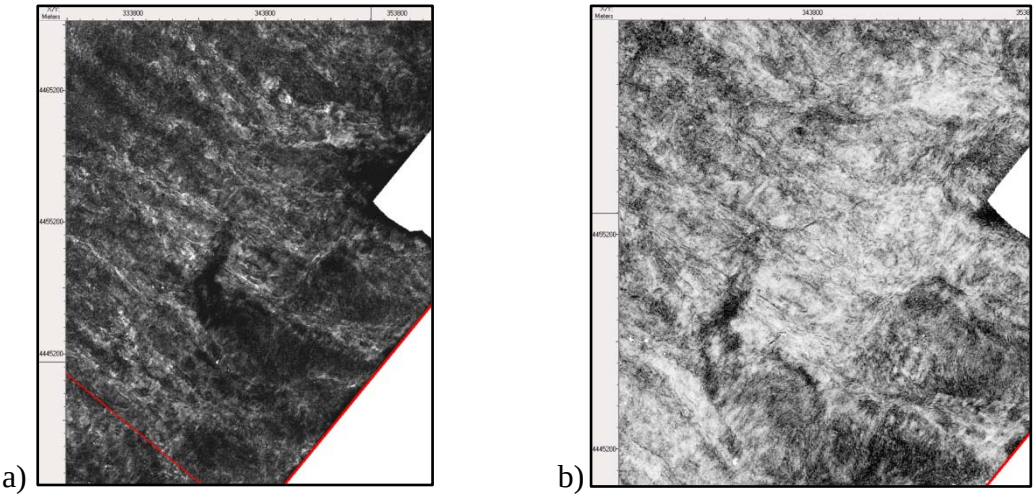

Fig. 35. Banded region and subtle channels observed in both amplitude (a) and coherence (b) maps.

Coherence map (Fig. 47, Appendix A) displays north-south fault alignments in its shallowest region. Besides, the banded structures, as well as the channels observed in amplitude map, can also be located in the coherence map (Fig. 35.b). Along the most proximal sector, coherence values displays NNE-SSW fault alignments previously seen in Top Oligocene and PreMess1 coherence maps.

7.1.3.3. PreMess3

PreMess3 is the youngest studied pre-Messinian horizon. Located between 1.64 and 2.89 stwtt, this seismic surface is more restricted than the previous ones because a large part of the horizon is eroded by the MES (Fig. 31).

The time structure map (Fig. 48, Appendix A) of PreMess3showsa southeastern dipping surface with a steeper slope than that observed for older horizons. The intermediate region located between the two slope-breaks in PreMess1 and 2, has now reduced its area and present a greater slope, creating a much steeper general relieve than the previous analyzed horizons.

Subunit-C is truncated at its top by the Messinian erosional event, limiting the information about this interval. Nevertheless, a detailed observation of crosslines shows a significant sigmoidal shape. Internal reflectors display two different patterns (Fig. 36). The bottom of the seismic package contains more or less parallel reflectors that continue the general trend to dip towards the southeast. However, at the top of the unit, the reflectors change their dip direction to the northwest, which might suggest a mainly

aggradational geometry in the topset region and subsequent landward tilting by latter sediment loading.

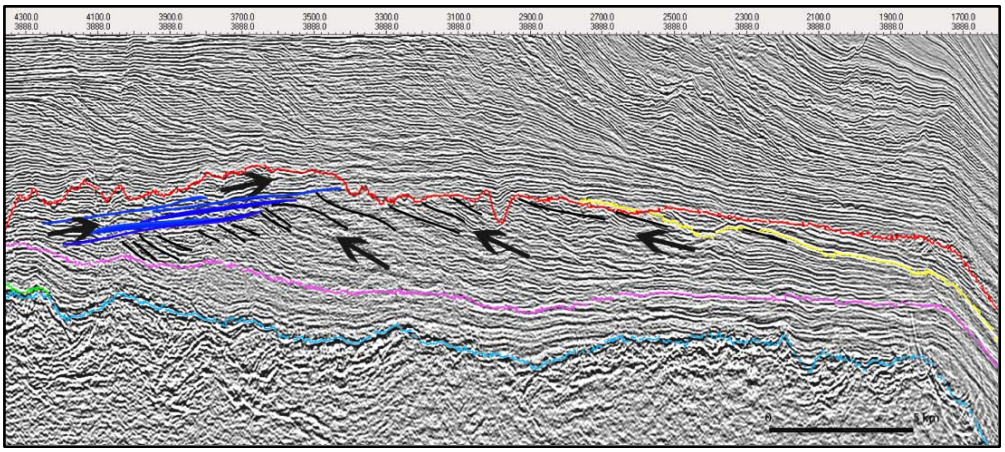

Fig. 36. Scheme showing the reflectors' tendency within Sb-C.

Seismic amplitude data (Fig. 49, Appendix A) displays some minor tributary systems that do not really correspond with this time level. They are consequence of the amplitude calculation methods, which were carried out from a volume (0.05 stwtt above and below the surface of interest), i.e. in those points where PreMess3 and MES are separated less than 0.05 stwtt, the amplitude result includes Messinian Surface data (Fig. 37). Therefore, most of the drainage structures seen in this map are not taken into account as belonging to this horizon.

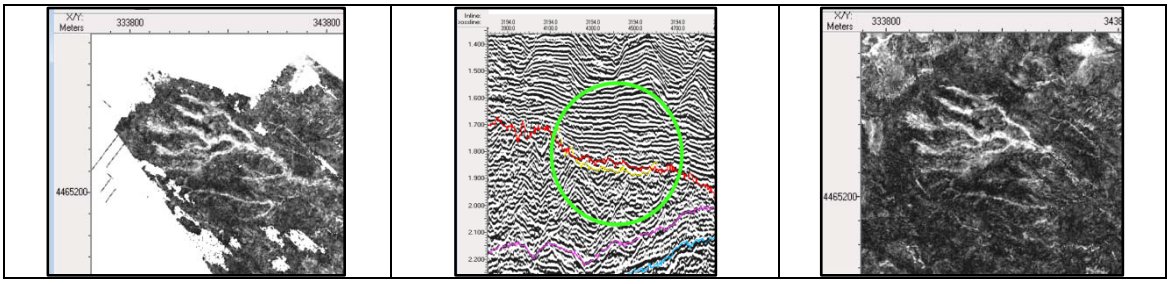

Fig. 37. Detail of the same zone in MES and PreMess1 amplitude maps. The horizon's reflectors are so close that amplitude values are combined, causing the record of the Messinian erosion on PreMess1 and displaying the same pattern of channels in both surfaces; a) Detail of PreMess1 amplitude map; b) Example of the proximity of both reflectors; c) Detail of MES amplitude map.

The coherence map shows a high coherence band parallel to the coastline located in the middle of the picked area. Seaward values become lower, enabling to observe some minor channels crossing the maximum vertical gradient zone (Fig. 50, Appendix A). These incisions continue the temporal trend of increasing canyon width

and depth seen in the previously described surfaces, particularly in the head region, as well as an increase in their spacing along the shelf-edge. In the upper part of the profile, channels and detritic systems belong to the Messinian Surface.

7.2. Isochoric maps of the Miocene Seismic Subunits

The depocentres are the areas of thickest deposition in a sedimentary basin. In order to study the evolution of these maximum sedimentation areas and their relation to the Messinian paleo-valleys, isochoric maps were obtained for each subunit.

- *Subunit-A*: It is limited to the northern third of the survey area. This seismic interval, between the acoustic basement and PreMess1, presents a depocentre located in the northern corner of the survey, coinciding with an area of lower elevation (Fig. 38.a). Southwards, the unit thickness progressively decreases until total pinch out.
- *Subunit-B*: This sedimentary package was deposited between PreMess1 and2. Since PreMess1 does not cover the entire survey area, the bottom boundary was generated as a surfaces composition. In those zones where PreMess1 does not exist, the corresponding bottom will be the Top Oligocene surface (Fig. 20).

  The resulting isochoric map (Fig. 38.b) presents a completely opposite distribution to that of the underlying sequence. The depocentre is placed in the southern sector of the survey. A secondary depocentre occurs associated with depressions in the Top Oligocene horizon. The northern zone is the one with a lower sediment accumulation.
- *Subunit-C*: The sedimentation that occurred between PreMess2 and PreMess3 was partially eroded by the MES. Thus the upper limit used to obtain the isochoric map is the composition between PreMess3 and the Messinian surface (Fig. 20) and represents a minimum accumulation. Thicknesses resulting from the calculation show a depocentre that is parallel to the Present-day coastline in the middle of the survey area. The depocentre is cut by a relative deep valley, which coincides with the Messinian Ebro River location (Fig. 38.c).

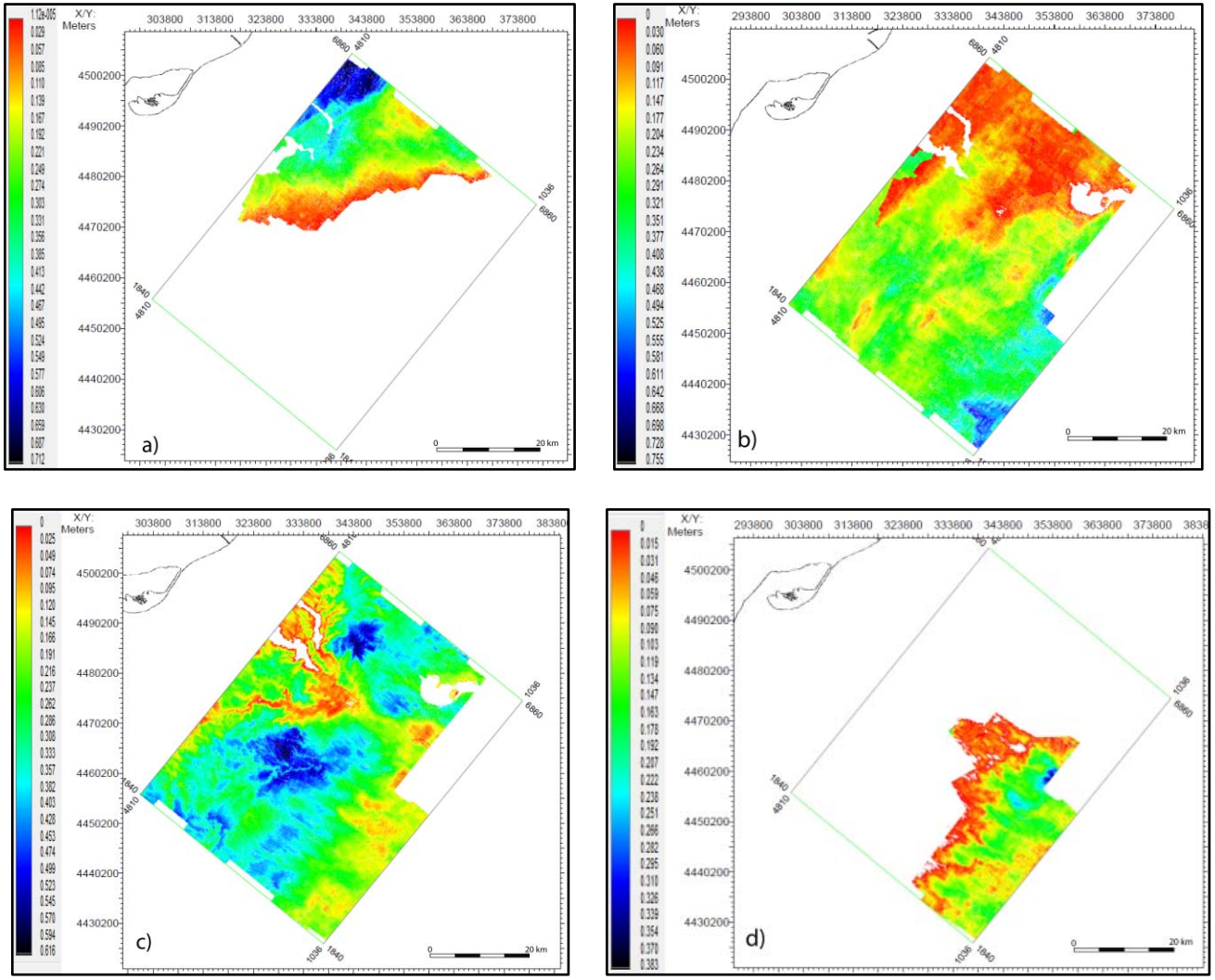

Fig. 38. Isochoric maps displaying sediment accumulation between the studied horizons: a) Sb-A, from acoustic basement to PreMess1; b) Sb-B, from PreMess1 and PreMess2; c) Sb-C, from PreMess2 to PreMess3; d) Sb-D, from PreMess3 to MES (thickness is in stwtt units).

An unknown thickness of the deposits was eroded by the MES, so the original depocentre distribution could be different to that found today. The maximum slope region shows medium sedimentary rates.

- *Subunit-D*: This seismic unit is delimited by the PreMess3 at the bottom and the MES at the top. In the same way as for the underlying package, it lost much of its thickness and real extent by erosion, surviving only the southern third of it. The higher accumulation area coincides with the end of the main drainage area of the Messinian Ebro River (Fig. 38.d).

Chapter 8

Discussion

8.1. Evolution of the Ebro Margin during the Miocene

Miocene evolution of the Ebro Margin was analyzed in detail to provide evidences of the existence of a precursor of the Ebro River. We found that the reflector at the top of the Oligocene sequence in the study area shows a major northeast oriented horst-and-graben structure (Fig. 25), developed in a strong extensional tectonic context during the upper Oligocene-Burdigalian (García-Siñeriz *et al.*, 1979; Sàbat *et al.*, 1997; Roca *et al.*, 1999). The listric normal faults, which generated this structure, present an ENE-WSW strike (Fig. 26) and southeastern dip.

The early Miocene sediments, coinciding with the Subunit-A in our work, were mainly controlled by the extensional fault system that was present during the late Paleogene to early Miocene. This seismic unit is characterized by parallel to sub-parallel seismic facies restricted to the deepest part of the graben troughs, as can be seen in Fig. 23, Fig. 24 and Fig. 39. These sediments are affected by normal faults, especially in those areas closest to the coastline, as can be observed in the coherence map (Fig. 44).This feature, combined with thickness variations towards the normal faults observed along the seismic profiles, support the idea that the syn-rift stage continued during the early-Miocene, as was previously described by Roca *et al.* (1999).Along the upper part of Sb-A a change in the seismic facies still affected by minor faults is observed from parallel to sigmoidal geometry. Only in the closest coastal grabens, sediments reach to infill the troughs due to the sediment supplies (Fig. 32, Fig. 38a and Fig. 39).

The subsequent seismic sequence, Sb-B, shows a clear sigmoidal clinoform that covers the entire survey area. Seismic facies within this interval present wavy morphologies, which typically display dip amplitude variations on amplitude maps (Fig. 35) possibly related to channel-levee systems and other sediment pathways. During this time, deposits continued totally or partially filling the grabens, spreading over the

structural highs and onlapping the morphology (Fig. 38.b). The general NW-SE surface dipping, together with the reflector's toplap geometry, are characteristic of a prograding sequence (Fig. 34).

The evolution of this progradation system is characterized by offshore faults coating and the smoothing of the margin morphology. During this process, sediments were accumulated modifying the shelf morphology: 1) flattening the topset; b)softening the offset, and c)decreasing the slope of the foreset zone (Fig. 34).Thus, the sediment transport increasingly moved in the southwest direction, longitudinally from the coastline (Fig. 38 and Fig. 39).Since the sedimentary facies do not change their thickness and are only deformed in their lower parts by the faults, we might think that this evolution took place during a soft transition between the syn-rift and the post-rift stages. This trend continues, even intensifies, in the overlaying sequence (Sb-C).

The youngest of the seismic packages (Sb-D), though incomplete, seems to maintain the sigmoidal morphology trend at its bottom. However reflectors at the top of the unit change their dip direction to the NW, suggesting a transition from a progradational to a aggradational system (Fig. 36), and denoting almost total attenuation of the tectonic activity. During this period, some minor sediment pathway structures are located along the foresets of the prograding clinoforms (Fig. 37). The isochoric map of the unit shows an offshore shift of the depocentre (Fig. 38.d and Fig. 39), so it would be logical to think that between deposition of PreMess2 and the MSC, sediment transport direction changed sometime from the north-northwest (longitudinal) to the east-northeast (transversal to the coastline).

During the Messinian Salinity Crisis the sea level in the Mediterranean dropped drastically between 1500 and 2700 m (Ryan, 1976; Meijer *et al.*, 2005; Blanc, 2006; Ryan 2008), resulting in subaerial exposure of large portions of submarine margin of the Western Mediterranean Sea. Indicative features of this subaerial exposure of the Ebro Margin including the detritic character of the drainage network (Fig. 27, Fig. 28 and Fig. 29) or the meandering channels (Fig. 28.b,c) are displayed in Messinian amplitude and coherence maps. The Messinian Ebro Margin was dominated by a major fluvial valley (Fig. 28) identified by Urgeles *et al.* (2010) as the paleo-Ebro River, dissecting the Messinian paleo-relief perpendicularly to the present coastline. Three major physiographic regions, forming a flat-step-flat-step profile, characterize this surface.

The boundary between the two most distal regions, where most streams disappear, seems to be the limit of a base level.

8.2. Evidences for a pre-Messinian Ebro River

The timing and processes leading to the opening of the Ebro Basin towards the Mediterranean Sea is still under discussion. The seismic data analyzed in this work provide evidence supporting the idea of Arche (2002), García-Castellanos *et al.* (2003) and, more recently, Arche *et al.* (2010) or Urgeles *et al.* (2010), concerning to a pre-Messinian connection between the Ebro Basin and the Mediterranean through a proto-Ebro River.

Our seismic data volume clearly shows that the Messinian event temporally truncated the evolution of the Ebro Margin in the later Miocene, deeply cutting into the underlying pre-Messinian clinoform package. It is remarkable the presence of a major valley dissecting the MES from NE to SW with some third/forth order tributaries with sinuosity about 1.3, according to the classification of Urgeles *et al.* (2010).The channel width varies between 300 m and 1 km, while the tributaries width is lesser than 300 m. These features, included some abandoned meanders, are recognized in both amplitude and coherence maps (Fig. 28 and Fig. 29).

By observing the carved valley in the amplitude and coherence maps of the MES, we think that it would have been difficult for a proto-Ebro river to have sufficient time to have cut across a mountain range and to attain the equilibrium conditions suggested by the meandering nature and the low gradient during the Messinian (Fig. 28b).So, the great developed of this drainage network suggest that the capture of the Ebro Basin by a relative small river have to occur prior to the Messinian drawdown.

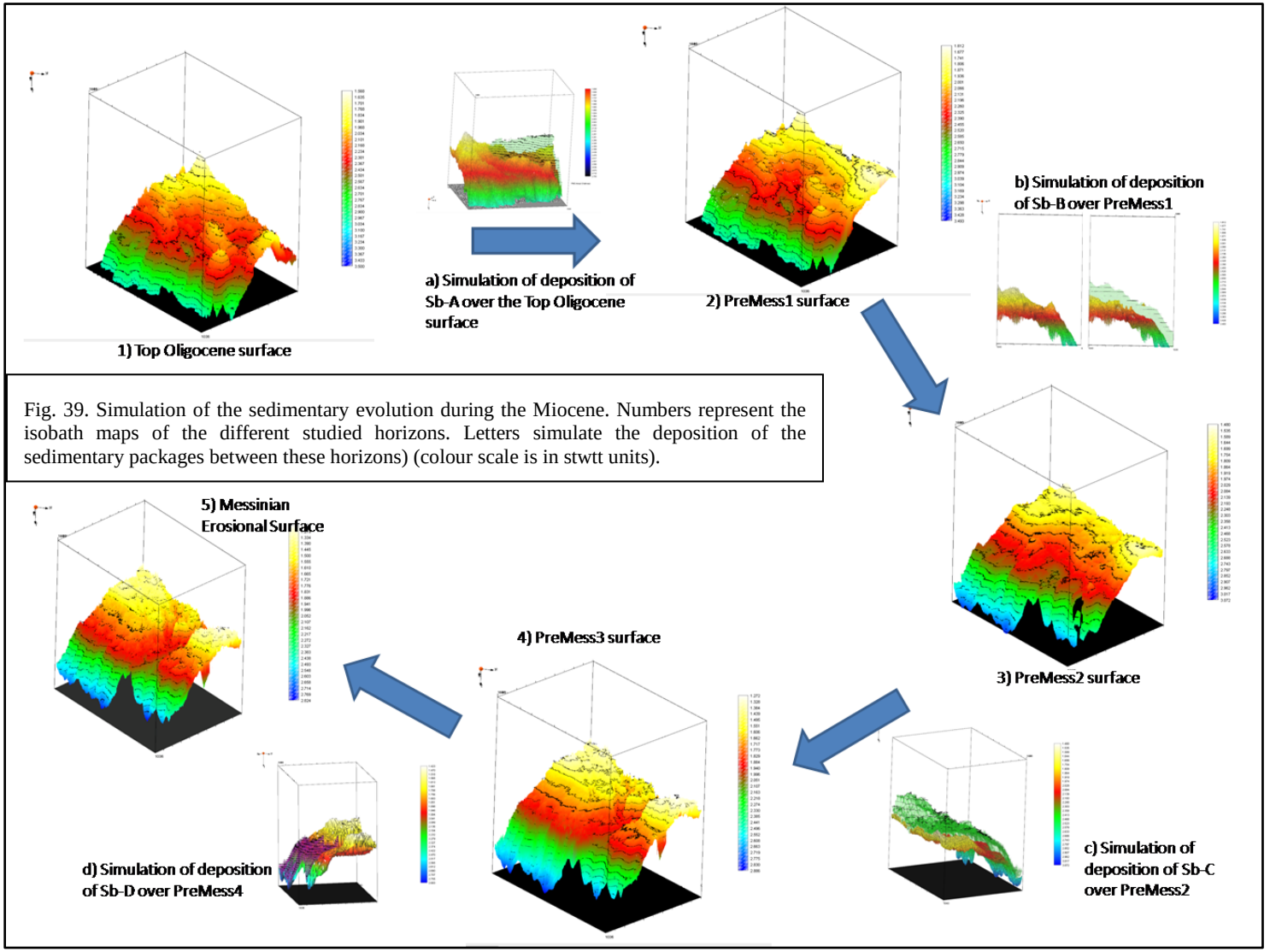

Fig. 39. Simulation of the sedimentary evolution during the Miocene. Numbers represent the isobath maps of the different studied horizons. Letters simulate the deposition of the sedimentary packages between these horizons) (colour scale is in stwtt units).

On the other hand, the beginning of sediment accumulation coeval with the extensional period (Sb-A), is characterized by the restriction of the deposits to the northeastern graben troughs during the Lower Miocene (Fig. 38 and Fig. 39). The evolution of the margin during deposition of Sb-B and Sb-C derived in the Castellon Group basinward-prograding megasequence (Serravallian-Tortonian), according to the terminology of Frey-Martinez *et al.* (2004) and Bertoni and Cartwright (2005), and identified from the industry well data (Lanaja *et al.*, 1987). Between these two packages, an increase in the volume of sedimentary contributions can be observed from the 3D seismic data, since the time interval to both units is the same but the thickness of the Sb-A is remarkably lesser than this of the Castellon Group.

Also, clinoforms geometries deposited between PreMess1 and PreMess3 (Fig. 23 and Fig. 24) suggest that the progradation was comparable to that which occurred during the Plio-Pleistocene (Bartrina *et al.*, 1992; Roca *et al.*, 2001; Urgeles *et al.*, 2010). Anyway, depocentre evolution shows a shift southwestward, indicating a change in the sediment transport from longitudinal (N-NW) to transversal (E-NE) (Fig. 38 and Fig. 39). This suggests a change in the sedimentary focus, probably from a predominant marine supply, to a focus associated to the coastal area. This increase of the sediment rate, together with the change in the transport direction is presumably indicative of the existence of a pre-Messinian Ebro River.

Chapter 9

Conclusions

Three-dimensional (3D) seismic reflection is a non-invasive geophysical method that has allowed us to study geological structures beneath the seafloor in sensitive areas such as the Ebro Margin. It has provided high-resolution underground images to detect geologic formations that are not apparent using conventional techniques, such as faults or erosional truncations. The implementation of seismic attributes, such as amplitude or coherence, has improved our capacity to visualize and interpret features such as sedimentary patterns (e.g., channel systems) or faults and fractures in any orientation.

This 3D seismic reflection survey has allowed us to determine that the Ebro Margin has been controlled by tectonic evolution, sea-level changes, sediment supply and the connection of the Mediterranean with the Atlantic. This main idea has is associated with the following conclusions:

1) The actual Ebro Margin is a major NE-SW oriented horst-and-graben structure developed in an extensional context and bounded by NE-SW normal faults. This geomorphology controlled the sedimentary evolution of the area during the syn-rift stage (Lower Miocene), restricting the sediments to the deepest part of the graben troughs.

2) The increase of the sediment supply observed in the Castellon Group megasequence, involved in a progressive filling of the grabens, subsequent spreading and final onlapping of the structural highs which surrounded the troughs. This caused the development of sigmoidal clinoform facies with distinct topset, foreset and bottomset, characteristic of a prograding sequence. These stratigraphic sequences were slightly affected by the fault activity, suggesting waning rifting activity during the Serravallian-Tortonian period. This increase in sedimentation rate was responsible of a progradation comparable to that occurred during the Plio-Pleistocene and must be

associated with a depositional focus as a proto-Ebro River draining from the Ebro Basin.

3) The study of the depocentres indicates that, during the Lower Miocene the sediment transport was mainly from the N-NW. Coinciding with the increase of the sediment supply, there was a shift in the transport direction, changing from longitudinal (N-NW) to transversal (E-NE) and suggesting a sediment focus associated with the coastline such as the proto-Ebro river.

4) The Messinian Salinity Crisis temporarily truncated the evolution of the Ebro Margin, removing part of the existing Miocene record. This event cut deeply into the underlying pre-Messinian clinoform package with a great valley identified as the paleo-Ebro River. The major channel width, the sinuosity of the drainage system, as well as the existence of some abandoned meanders, suggest that a relative small river would not have enough time to reach equilibrium conditions if the capture of the Ebro Basin have not occurred prior to the Messinian Salinity Crisis.

Bibliography

Alonso, B., Field, M. E., Gardner, J., & Maldonado, A. (1990). Sedimentary evolution of the Pliocene and Pleistocene Ebro margin, northeastern Spain. *Marine Geology , 95*, 313-331.

Arche, A., Evans, G., & Clavell, E. (2010). Some considerations on the initiation of the present SE Ebro river drainage system: Post- or pre-Messinian? *Journal of Iberian Geology , 36*, 73-85.

Avseth, P., Mukerji, T., & Mavko, G. (2005). *Quantitative Seismic Interpretation: Applying Rock Physics Tools to Reduce Interpretation Risk.* Cambridge: Cambridge University Press.

Babault, J., Loget, N., Van Der Driessche, J., Castelltort, S., Bonnet, S., & Davy, P. (2006). Did the Ebro basin connect to the Mediterranean before the Messinian salinity crisis? *Geomorphology , 81*, 155-165.

Bakker, P. (2002). *Image structure analysis for seismic interpretation.* Technische Universiteit Delft. ASCI dissertation series number 78.

Bartina, M., Cabrera, L., Jurado, M., Guimerà, J., & Roca, E. (1992). Evolution of the central Catalan margin of the Valencia Trough (western Mediterranean). *Tectonophysics* (203), 219-247.

Bartolomé, R. (2002). *Evolución tectónica del margen continental oeste de México: Fosa Mesoamericana y Golfo de California.* Universitat de Barcelona. Unpublished PhD thesis.

Bertoni, C., & Cartwright, J. (2005). 3D seismic analysis of slope-confined canyons from the Plio-Pleistocene of the Ebro Continental Margin (Western Mediterranean). *Basin Research , 17*, 43-63. doi: 10.1111/j.1365-2117.2005.00254.x.

Blanc, P. (2006). Improved modelling of the Messinian Salinity Crisis and conceptual implications. *Palaeogeogr. Palaeoclimatol. Palaeoecol.* (238), 349-372. doi: 10.1016/j.palaeo.2006.03.033.

British Geological Survey. (n.d.). *BGS Research - CO2 storage at the Sleipner field*. Retrieved August 15, 2010, from British Geological Survey Web site: http://www.bgs.ac.uk

Caldwell, J., & Dragoset, W. (2000). Brief overview of seismic air-gun arrays. *Leading Edge (Tulsa, OK) , 19* (8), 898-902.

Clauzon, G. (1982). Le canyon messinien du Rhône: une prevue decisive du "desiccated deep-basin model". *Bull. Soc. Geol. Fr.* (24), 597-610.

Clauzon, G., Suc, J., Gautier, F., Berger, A., & Loutre, M. (1996). Alternate interpretation of the Messinian salinity crisis: controversy resolved? *Geology* (24), 363-366.

Chaouch, A., & Mari, J. (2006). 3-D Land Seismic Surveys: Definition of Geophysical Parameters. *Oil & Gas Science and Technology - Rev. IFP , Vol. 61, No. 5*, 611-630. doi: 10.2516/ogst:2006002.

Chopra, S., & Marfurt, K. (2007). *Seismic Attributes for Prospect Identificatin and Reservoir Characterization* (Vol. Geophysical Developments No.11). Society of Exploration Geophysicists.

Dañobeitia, J., Alonso, B., & Maldonado, A. (1990). Geological framework of the Ebro continental margin and surrounding areas. *Marine Geology , 95 (3-4)*, 265-287.

dGB Beheer B.V. (2009). *OpendTect User Documentation version 4.0.* User's Manual, dGB Beheer B.V.

Dorn, G. (1998). Modem 3-D seismic interpretation. *Leading Edge (Tulsa, OK) , 17* (9), 1292.

Dragoset, B. (2000). Introduction to air guns and air-gun arrays. *The Leading Edge , Vol.19, No.8*, 892-897. doi: 10.1190/1.1438741.

Duggen, S., Hoernie, K., Van Bogaar, P., Rupke, L., & Moran, J. (2003). Deep roots of the Messinian salinity crisis. *Nature* (422), 602-606.

Escutia, C., & Maldonado, A. (1992). Paleogeographic implications of the Messinian surface in the Valencia Trough, northwestern Mediterranean Sea. *Tectonophysics* (203), 263-284.

Evans, G., & Arche, A. (2002). The flux of siliciclastic sediment from the Iberian Peninsula, with particular reference to the Ebro. *Geological Society Special Publication , 191*, 199-208.

Fre-Martínez, J., Cartwright, J., Burgess, P., & Vicente-Bravo, J. (2004). 3D seismic interprettion of the Messinian Unconformity in the Valencia Basin, Spain. (J. C. R.J. Davies, Ed.) *3D Seismic Technology: Application to the Exploration of Sedimentary Basins* , 91-100.

García-Castellanos, D., Estrada, F., Jiménez-Munt, I., Gorini, C., Fernández, M., Vergés, J., et al. (2009). Catastrophic flood of the Mediterranean after the Messinian salinity crisis. *Nature , 462 (7274)*, 77-781. doi: 10.1038/nature08555.

García-Castellanos, D., Vergés, J., Gaspar-Escribano, J., & Cloetingh, S. (2003). Interplay between tectonics, climate, and fluvial transport during the Cenozoic evolution of the Ebro Basin (NE Iberia). *J. Geophys. Res. , 108 (B7)*, 2347. doi: 10.1029/2002JB002073.

García-Siñeriz, B., Querol, R., Castillo, F., & Fernandez, J. (1979). A new hydrocarbon province in the western Mediterranean. *10th World Petroleum Congress, Bucharest* (pp. 191-197). London: World Petroleum Congress, Bucharest (Rumania).

Geel, T. (1995). Oligocene to early Miocene tectono-sedimentary history of the Alicante region (se spain): Implications for Western Mediterranean evolution. *Basin Research , 7* (4), 313-336.doi: 10.1111/j.1365-2117.1995.tb00120.x.

Hardage, B. (2010, July). Instantaneous Seismic Attributes Calculated by the Hilbert Transform. Article #40563 (2010). *Search and Discovery* . AAPG Datapages.

Hsü, K., Ryan, W., & Cita, M. (1973). Late Miocene desiccation of the Mediterranean. *Nature , 242*, 240-244.

Ikelle, L., & Amundsen, L. (2005). *Introduction to Petroleum Seismology (Investigations in Geophysics No.12).* Society of Exploration Geophysicists.

International Association of Geophysical Contractors [IAGC]. (March 2002). *Marine Seismic Operations. An overview.* Report, International Association of Geophysical Contractors [IAGC].

Kennett, N. (1983). *Seismic Wave Propagation in stratified Media.* Cambridge: Cambridge University Press.

Kertznus, V., & Kneller, B. (2009). Clinoform quantification for assessing the effects of external forcing on continental margin development. *Basin Research , 21*, 738-758. doi: 10.1111/j.1365-2117.2009.00411.x.

Krijgsman, W., Hilgen, F., Raffi, I., Sierro, F., & Wilson, D. (1999). Chronology, causes and progression of the Messinian salinity crisis. *Nature* (400), 652-655.

Lanaja, J., Querol, R., & Navarro, A. (1987). *Contribución de la exploración petrolífera al conocimiento de la Geología de España.* Madrid: Instituto Geológico y Minero de España.

Landro, M., & Amundsen, L. (2010, March 16). *Marine Seismic Sources II: Geoexpro.* (N. -2. GEO ExPro Magazine Vol. 7, Ed.) Retrieved July 20, 2010, from GeoExPro. Geoscience & Technology Explained: http://www.geoexpro.com

Landro, M., & Amundsen, L. (2010, February 18). *Marine Seismic Sources: Geoexpro.* (N. -2. GEO ExPro Magazine Vol.7, Ed.) Retrieved July 20, 2010, from GeoExPro. Geoscience & Technology Explained: htt://www.geoexpro.com

Lofi, J., Gorini, C., Berne, S., Clauzon, G., DOs Reis, A., Ryan, W., et al. (2005). Erosional processes and paleo-environmental changes in the western Gulf of Lions (SW France) during the Messinian Salinity Crisis. *Marine Geology* (217), 1-30.

Loget, N., & Van Den Driessche, J. (2006). On the origin of the Strait of Gibraltar. *Sedim. Geol.* (188-189), 341-356.

Luzón, A., Pérez, A., Soriano, M., & Pocoví, A. (2008). Sedimentary record of Pleistocene paleodoline evolution in the Ebro Basin (NE Spain). *Sedimentary Geology , 205* (1-2), 1-13. doi: 10.1016/j.sedgeo.2008.01.004.

Maillard, A., Gorini, C., Mauffret, A., Sage, F. L., & Gaullier, V. (2006). Offshore evidence of polyphase erosion in the Valencia Basin (Northwestern Mediterranean): Scenario for the Messinian Salinity Crisis. *Sedimentary Geology , 188-189; doi: 10.1016/j.sedgeo.2006.02.006*, 69-91.

Maldonado, A., & Nelson, C. (1988). Dos ejemplos de márgenes continentales de la Península Ibñerica: El márgen del Ebro y el Golfo de Cádiz. *Rev. Soc. Geol. España , I*, 317-325.

Maldonado, A., & Nelson, C. (1990). The Ebro margin study, northwestern Mediterranean Sea. An introduction. *Marine Gology , 95*, 157-163.

Marsset, B., Missiaen, T., De Roeck, Y., Noble, M., Versteeg, W., & Henriet, J. (1998). Very high resolution 3D marine seismic data processing for geotechnical applications. *Geophysical Prospecting , 46*, 105-120.

Nelson, C., & Maldonado, A. (1990). Factors controlling late Cenozoic continental margin growth from the Ebro Delta to the western Mediterranean deep sea. *Marine Geology , 95*, 419-440.

Offshore Energy Environmental Research Association [OEER]. (n.d.). *Background Information on Research Areas.* Retrieved July 20, 2010, from Offshore Energy Research: http://offshoreenergyresearch.ca/

Olivet, J. (1996). La cinématique de la plaque ibérique. *Elf Aquitaine Production* (20), 131-195.

Riba, O., Reguant, S., & Villena, J. (1983). Ensayo de síntesis estratigráfica y evolutiva de la cuenca terciaria del Ebro. In J. Comba (Ed.), *Libro Jubilar J. M. Ríos, Geología de España* (pp. 131-159). Madrid: Instituto Geológico y Minero de España.

Rizzini, A., Vezzani, F., Cococcetta, V., & Milad, G. (1978). Stratigraphy and sedimentation of a Neogene-Quaternary section in the Nile Delta area. *Marine Geology* (27), 327-348.

Roca, E., Sans, M., Cabrera, L., & Marzo, M. (1999). Oligocene to Middle Miocene evolution of the central Catalan margin (northwestern Mediterranean). *Tectonophysics , 315*, 209-233.

Ryan, W. (1976). Quantitative evaluation of the depth of the Mediterranean before, during and after the late Miocene salinity crisis. *Sedimentology* (23), 791-813.

Sàbat, F., Roca, E., Muñoz, J., Vergés, J., Santanach, P., Masana, E., et al. (1997). Role of extension and compression in the evolution of the eastern margin of Iberia: the ESCI-Valencia trough seismic profile. *Rev. Soc. Geol. España* (8), 431-448.

SCAR Ad Hoc Group on marine acoustic technology and environment. (July 2002). *Impacts of Marine Acoustic Technology on the Antarctic Environment.* Report, Scientific Committee on Antarctic Research, SCAR Action Group on Acoustics.

Seismic Micro-Technology, Inc. (2008). *Kingdom Software User's Manual.* Houston, Texas: Seismic Micro-Technology, Inc.

Sheriff, R., & Geldart, L. (1995). *Exploration Seismology* (2nd ed.). Cambridge: Cambridge University Press.

Stampfli, G., & Höcker, C. (1989). Messinian paleorelief from a 3D seismic survey in the Tarraco concession area (Spanish Mediterranean Sea). *Geologie en Mijnbouw* (68), 201-210.

Stein, S., & Wysession, M. (2003). *An introduction to seismology, earthquakes, and earth structure.* Blackwell.

Taner, M. (2001). Seismic Attributes. *CSGE Recorder* , 48-56.

Taner, M., & Sheriff, R. (1977). *Application of Amplitude, Frequency, and Other Attributes to Stratigraphic and Hydrocarbon Determination: Section 2. Application of Seismic Reflection Configuration to Stratigraphic interpretation.* AAPG Memoir, 26.

Urgeles, R., Camerlenghi, A., García-Castellanos, D., De Mol, D., Garcés, M., Vergés, J., et al. (2010). New constraints on the Messinian sealevel drawdown from 3D seismic data of the Ebro Margin, western Mediterranean. *Basin Research* , doi: 10.1111/j.1365-2117.2010.00477x.

Urick, R. (1983). *Principles of Underwater Sound.* McGraw-Hill.

Verbeek, N., & McGee, T. (1995). Characteristics of high-resolution marine reflection profiling sources. *Journal of Applied Geophysics , 33* (4), 251-269.

Yilmaz, O. (2001). *Seismic data analysis* (Vol. I and II). (S. M. Doherty, Ed.) Tulsa: Soc. of Expl. Geophys.

Appendix I

Maps

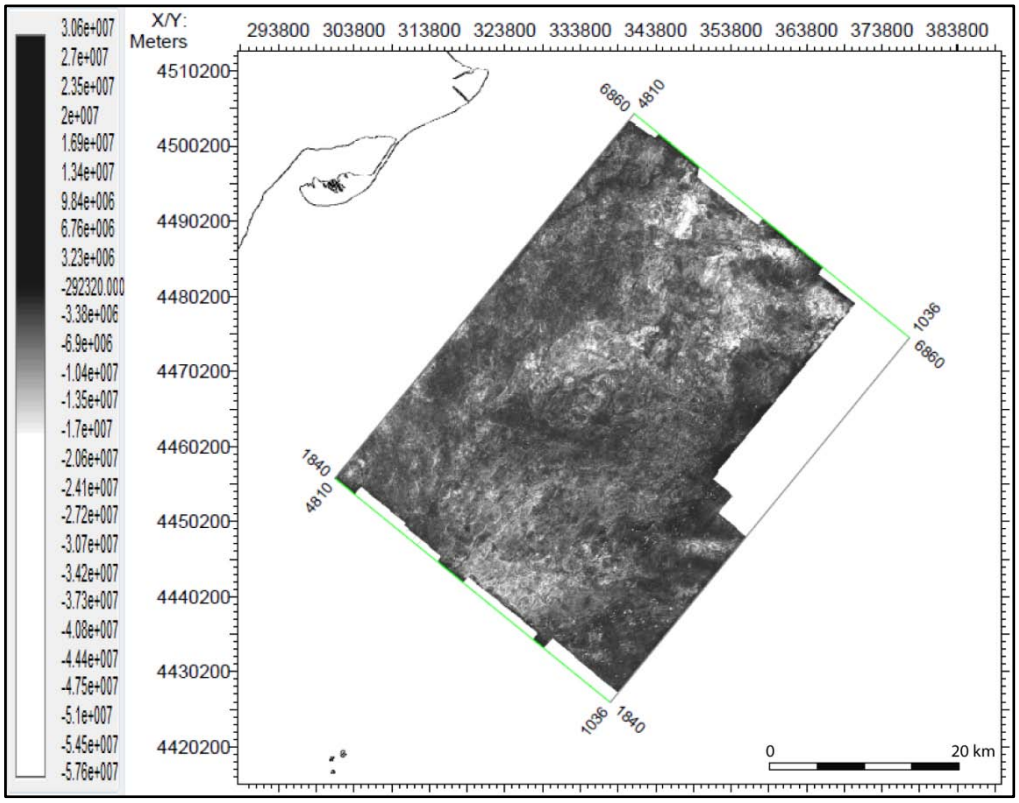

Fig. 40. Top Oligocene amplitude map

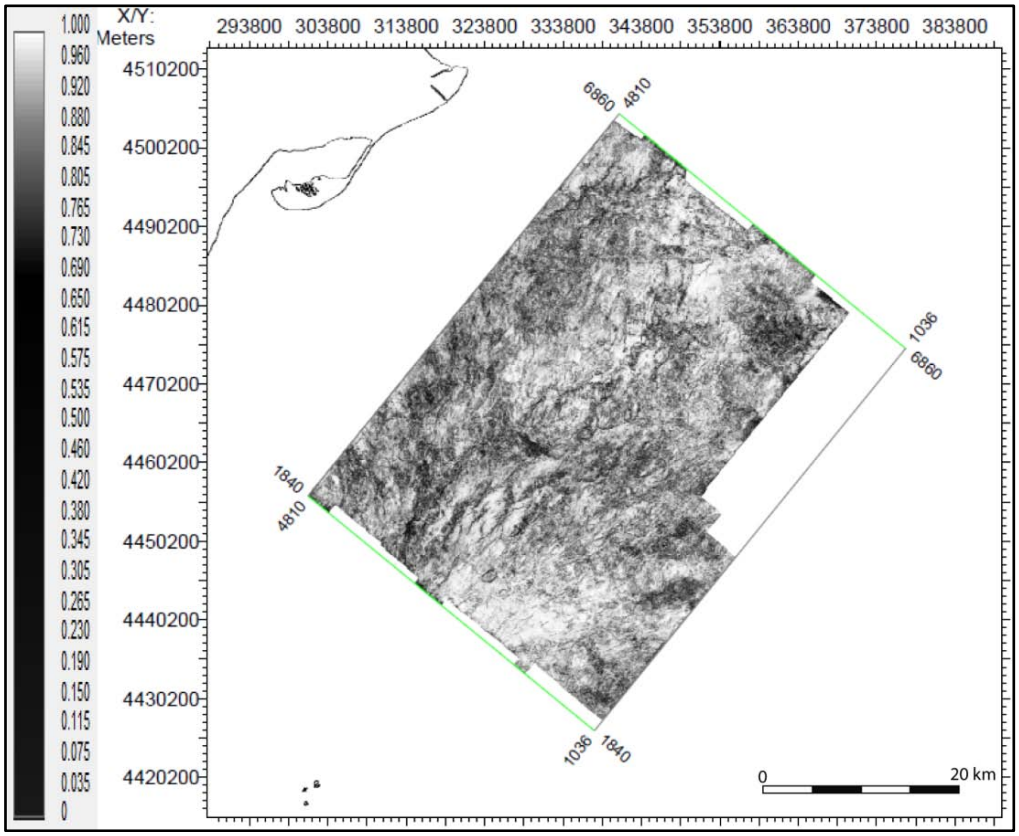

Fig. 41. Top Oligocene coherence map

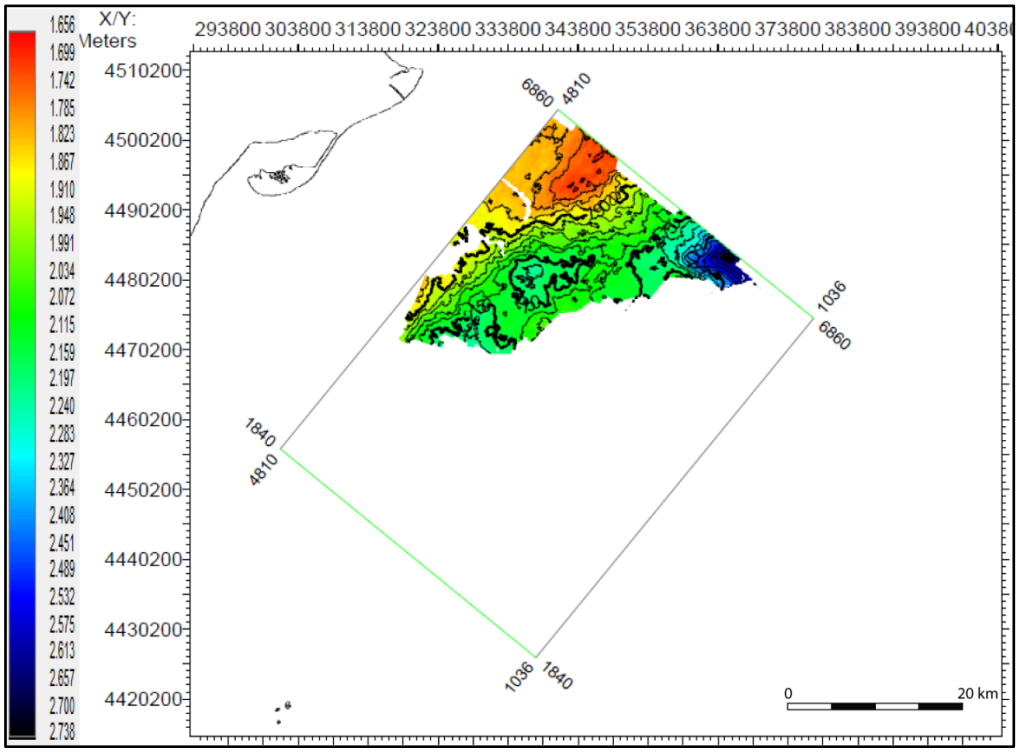

Fig. 42. PreMess1 isobath map (stwt units)

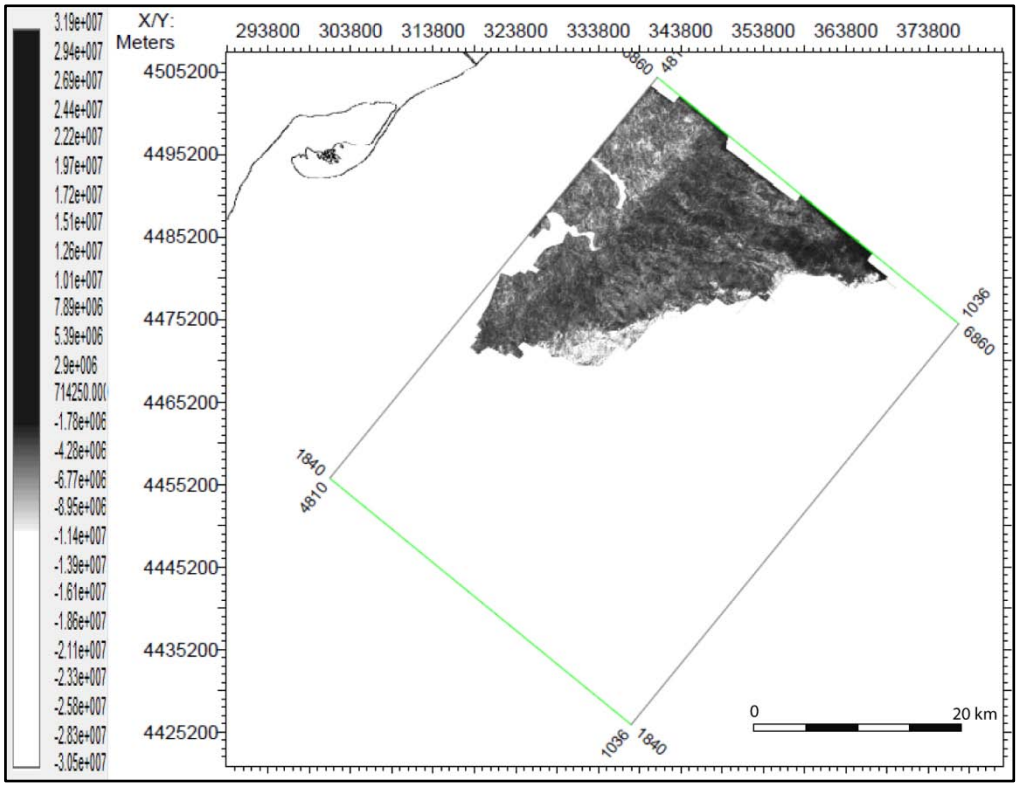

Fig. 43. PreMess1 amplitude map

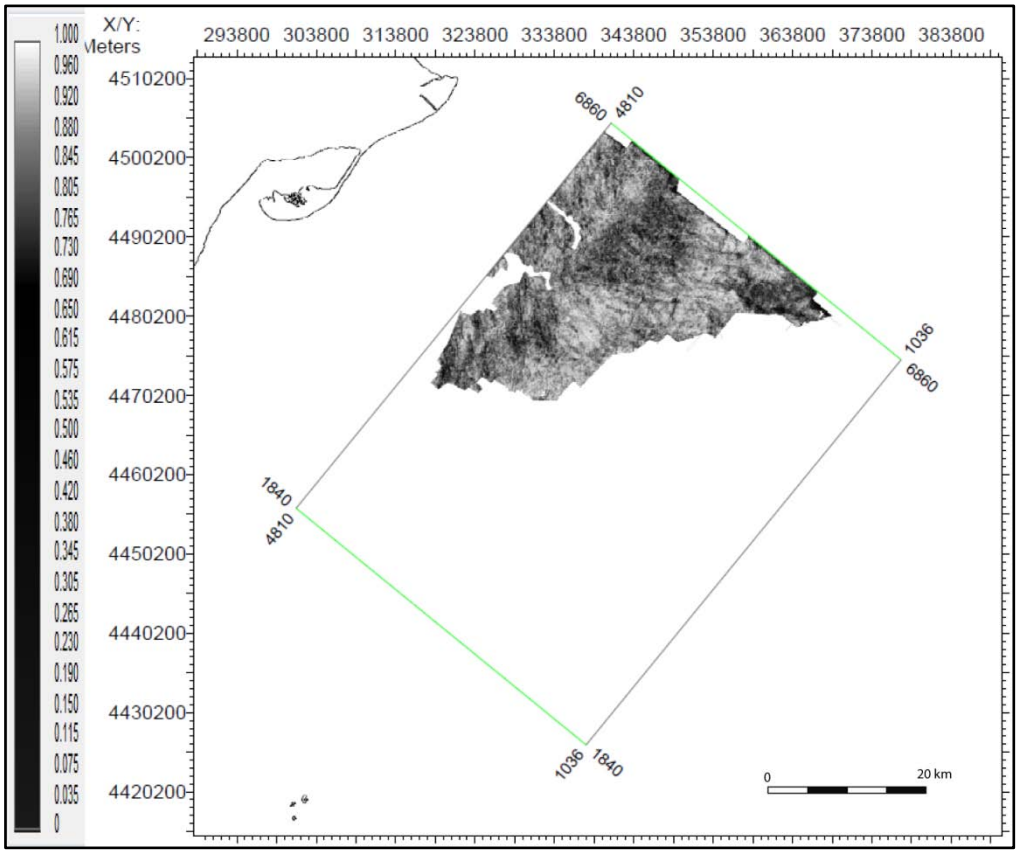

Fig. 44. PreMess1 coherence map

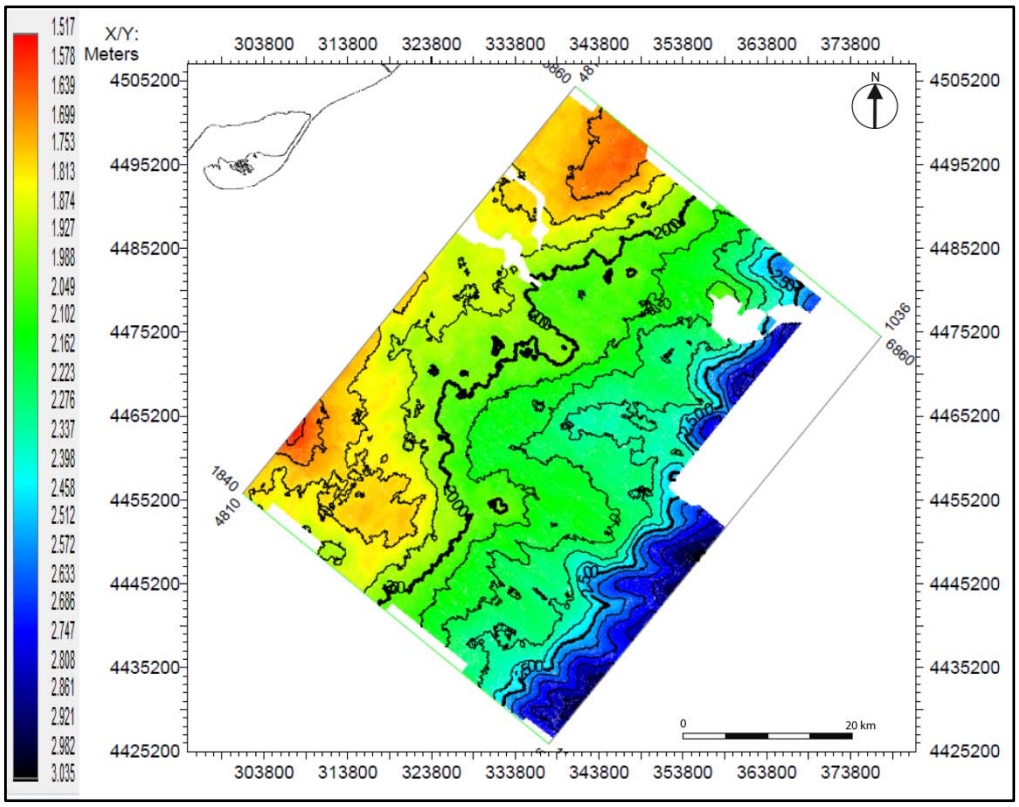

Fig. 45. PreMess2 isobath map (stwtt units)

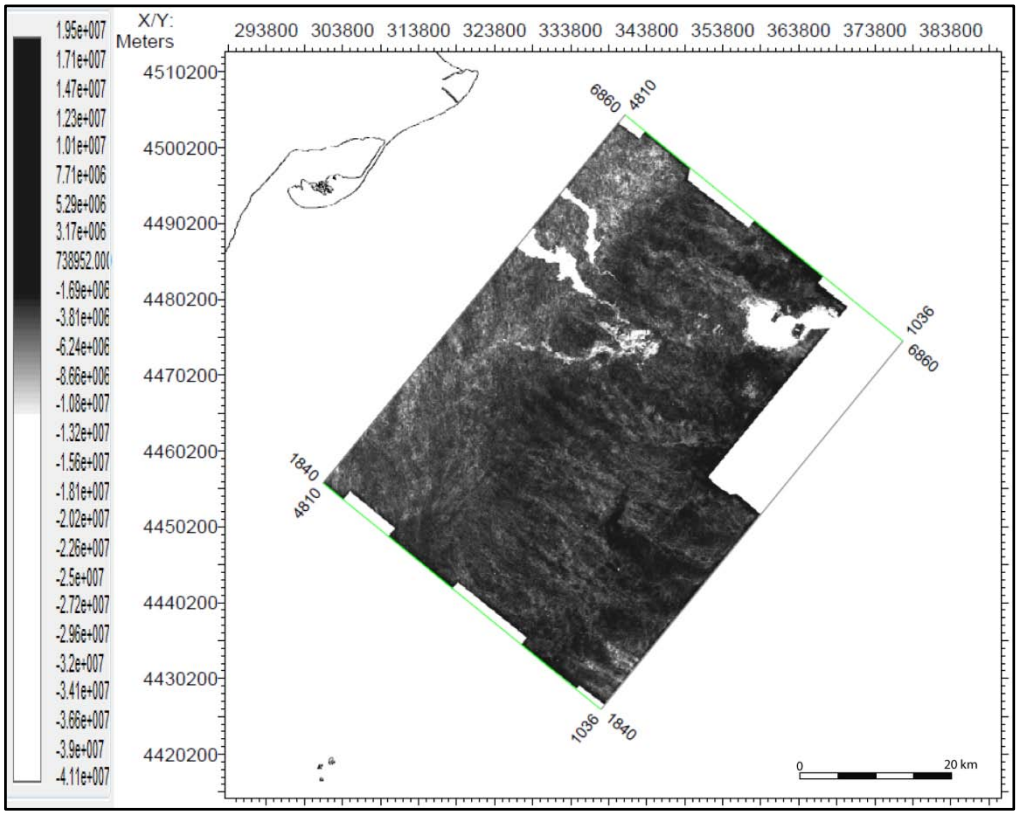

Fig. 46. PreMess2 amplitude map

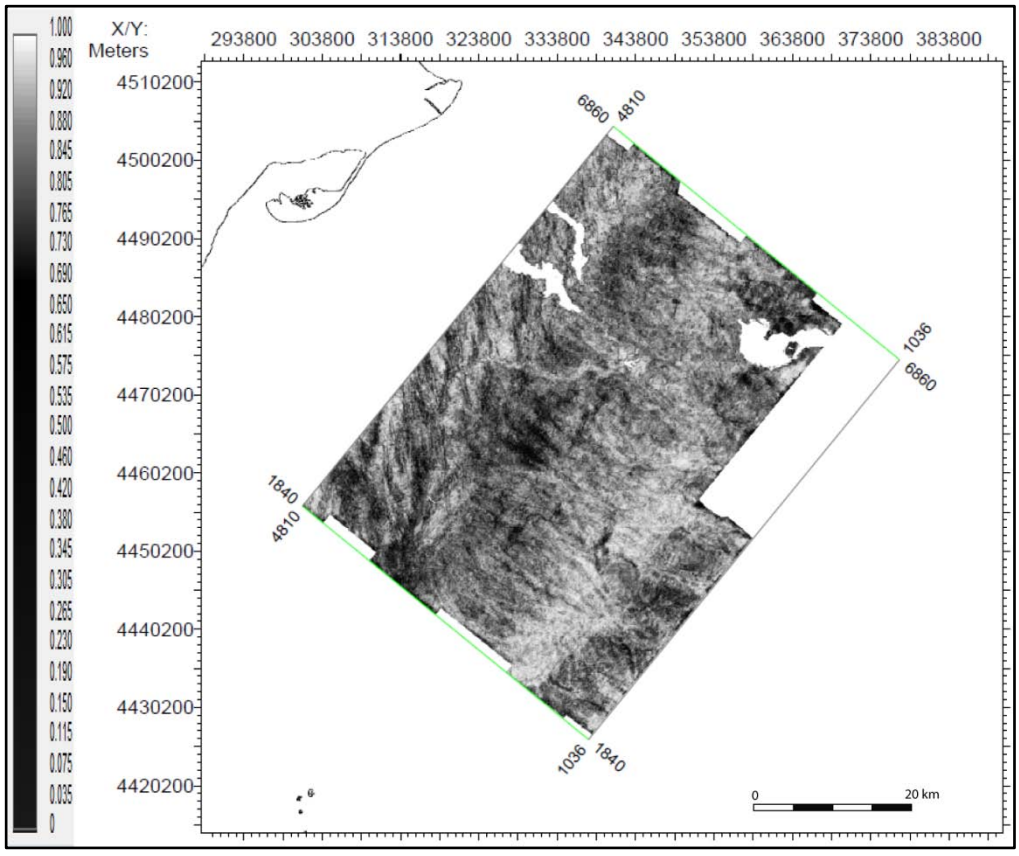

Fig. 47. PreMess2 coherence map

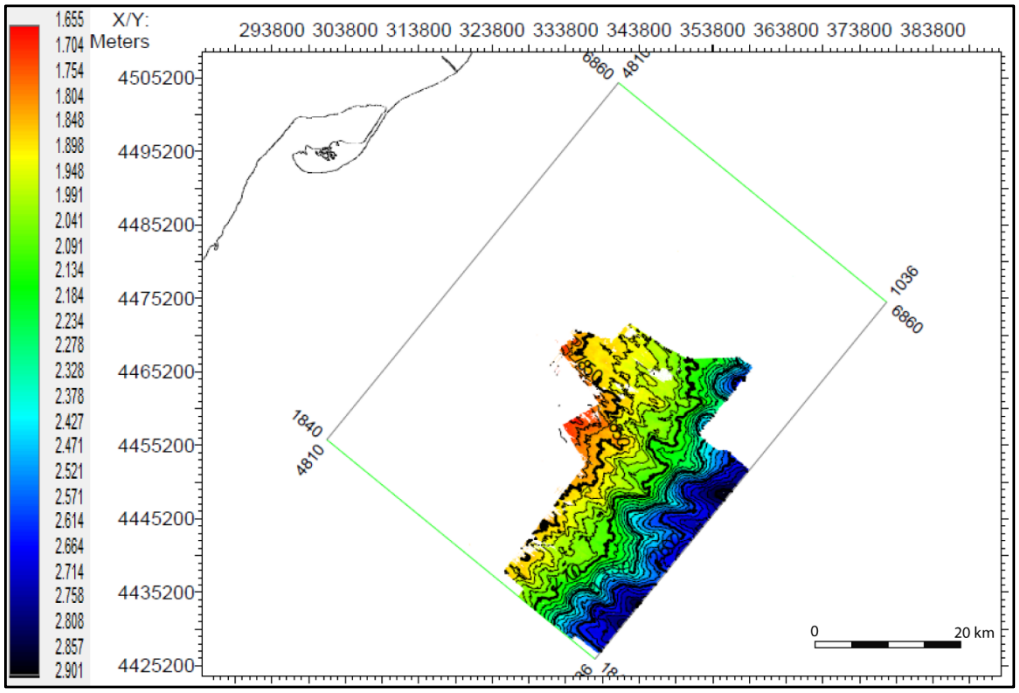

Fig. 48. PreMess3 isobath map

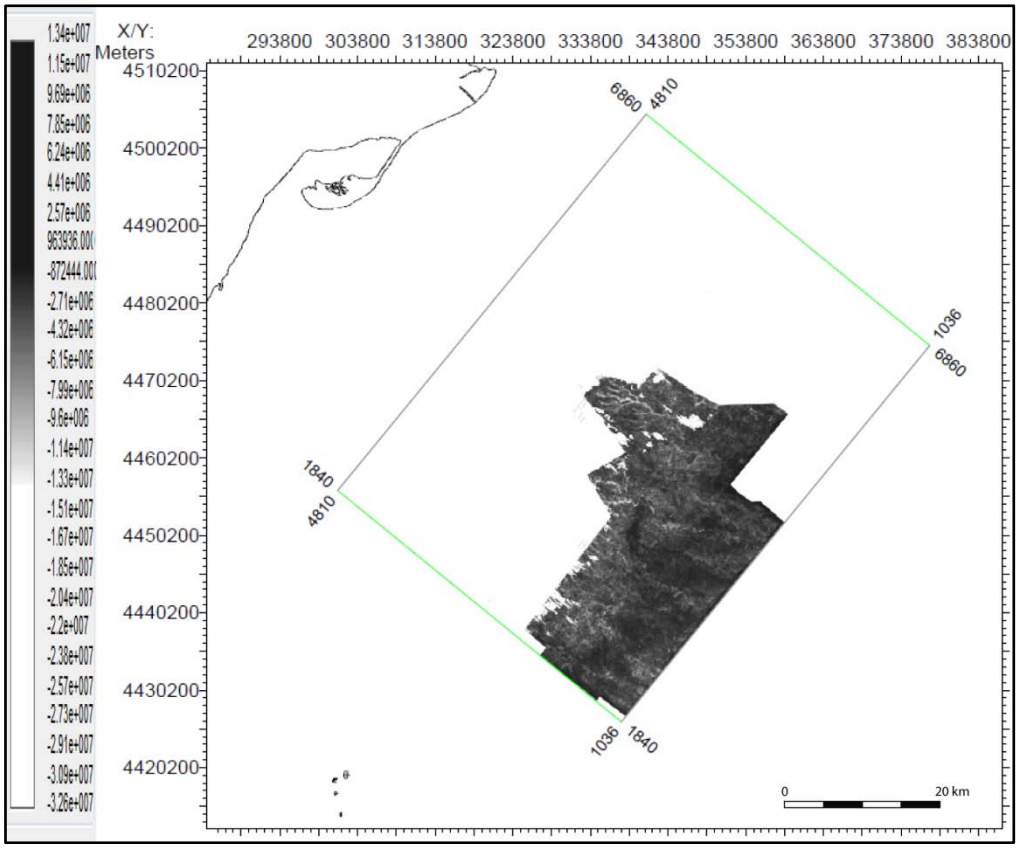

Fig. 49. PreMess 3 amplitude map

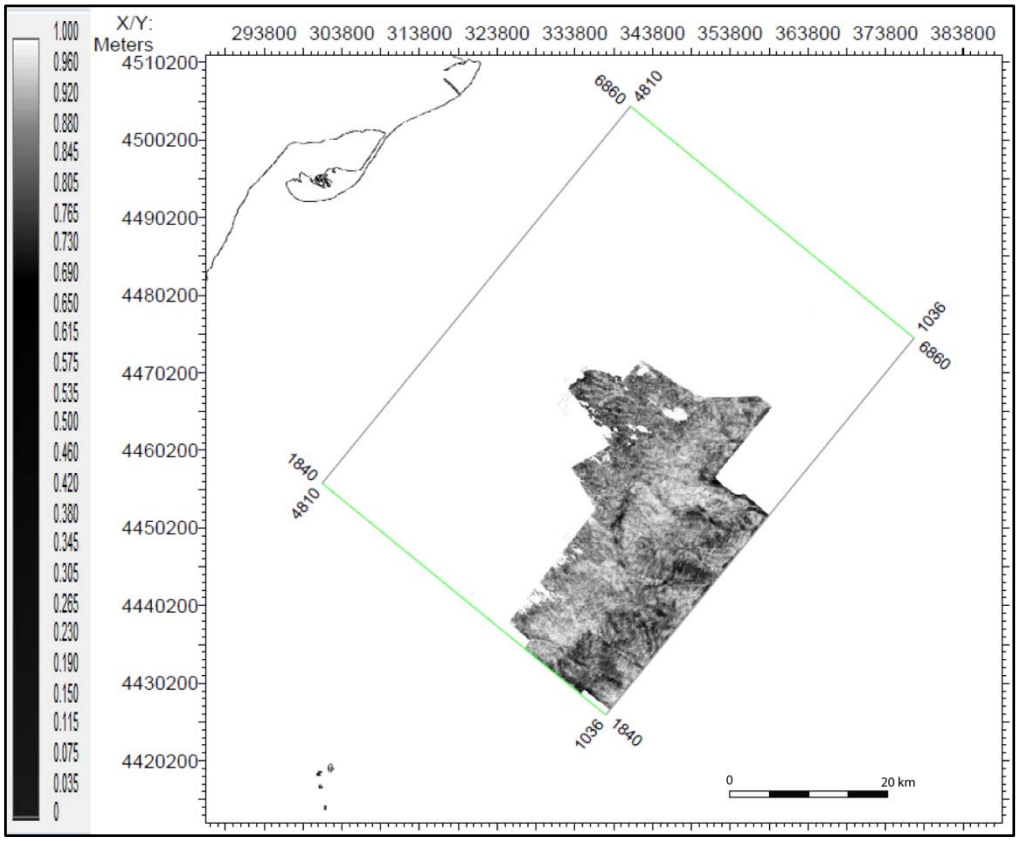

Fig. 50. PreMess 3 coherence map